e-ISSN 2757-5195

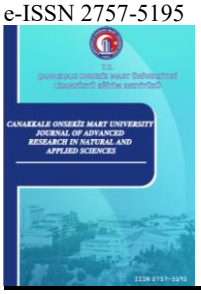

Çanakkale Onsekiz Mart University

Journal of Advanced Research in Natural and Applied Sciences

Open Access

doi.org/10.28979/jarnas.1186322 2023, Vol. 9, Issue 3, Pages: 670-687 dergipark.org.tr/tr/pub/jarnas

Bridging Molecular Docking to Molecular Dynamics to Enlighten Recognition Processes of Tailored Malononitrile Bearing D-A/D-A-D Types' AIEgens with HSA/BSA

Harun Nalçakan[1], Gülbin Kurtay[2,*]

[1]Department of Chemistry, Faculty of Science, Ankara University, 06100, Ankara, Türkiye
[2]Department of Chemistry, Faculty of Science, Hacettepe University, 06800, Ankara, Türkiye

Article History

Received: 09.10.2022

Accepted: 30.04.2023

Published: 20.09.2023

Research Article

Abstract − Fluorescence imaging-assisted photodynamic therapy (PDT) allows accurate tumor visualization and potentially prevents long-term side effects of cancer. Therefore, the development of photosensitizers emitting light, particularly in the near-infrared region (NIR), is essential for enhancing the efficacy of cancer therapy. On this premise, the formation of a stabilized complex between an organic dye and a target macromolecule improves fluorescence efficiency. In this scope, we performed a detailed molecular docking study of Donor (D)-Acceptor (A) *or* D-A-D type luminogens, all possessing malononitrile subunit with two blood proteins; namely bovine serum albumin (BSA) and human serum albumin (HSA), which appeared as robust carriers of several pharmaceuticals against preliminary cancer diseases. Our results revealed that the binding scores of the D_n-A_n *or* D_n-A_n-D_n:BSA complexes ranged from -8.50 to -11.70 kcal/mol while D_n-A_n *or* D_n-A_n-D_n:HSA complexes showed scores varying from -8.40 to -10.50 kcal/mol. Subsequently, molecular dynamics simulations were also performed for the best-docked ligands: macromolecule complexes; namely D_1-A_1:HSA, D_1-A_2:BSA and D_1-A_1-D_1:BSA to enlighten various structural parameters. Based on the predicted root-mean-square deviation (RMSD) values (on average), D_1-A_1:HSA complex was determined as 0.28 nm, D_1-A_2:BSA complex was determined as 0.25 nm. the D_1-A_1-D_1:BSA complex was found to be 0.32 nm, while the In addition, the root-mean-square fluctuations (RMSF) analyses (on average) revealed that D_1-A_1-D_1:BSA (0.152 nm) was slightly more flexible than D_1-A_1:HSA (0.16 nm).

Keywords *– BSA, HSA, luminogens, molecular docking, molecular dynamics, malononitrile.*

1. Introduction

Cancer is a disease characterized by uncontrolled cell division, and metastasis is the process through which cancer cells spread to other parts of the body. Metastatic cancer is widely recognized as one of the most significant risks to the general population's health, and this hazard has only gotten more severe throughout human history (Cox, 2021; Miller et al., 2019). Cancer treatments and diagnosis alternatives developed and used in contemporary medicine include surgery, chemotherapy, radiation, immunotherapy, and hormone therapy. The efficacy of these therapies varies according to the degree and kind of cancer. However, when these cancer therapies are used, significant side effects such as harm to healthy tissues or organs may occur (Debela et al., 2021).

Fluorescence imaging (FLI) assisted photodynamic therapy (PDT) has received significant interest in this context owing to its advantages over the aforementioned standard treatment approaches (Hishikawa et al., 2019; Rubtsova et al., 2021). These advantages include that it does not result in long-lasting side effects and allows for precise monitoring of drugs, tumor visualization, spatial and temporal particularity, and minimum invasive treatment. The mechanism of action of photodynamic therapy (PDT) is primarily based on photoexcitation of specially designed photoactive materials, also known as photosensitizers (PSs) (Escudero et al., 2021). These

[1] hnalcakan@ankara.edu.tr
[2] kurtay@science.ankara.edu.tr
[*]Corresponding Author

PSs are triggered by light at a specific wavelength and can undergo type-I or type-II photodynamic reaction pathways. These reaction pathways generate extremely cytotoxic reactive oxygen species (ROS) or singlet oxygen ($^1O_2$), respectively (Chakraborty et al., 2022; Chandra et al., 2022; Dewaele et al., 2010). Malignantly proliferating cells are destroyed by apoptosis (programmed cell death) or necrosis (non-programmed cell death) as a direct consequence of the production of these cytotoxic species (Mfouo-Tynga & Abrahamse, 2015). PSs can be activated photochemically and passes into an excited state when exposed to various light sources, including the visible and near-infrared (NIR) spectrum, which is the region of interest. Therefore, it is of utmost relevance at this step to create photosensitizers that emit at wavelengths in the near-infrared region (NIR), where it is more probable to have superior penetration effectiveness, particularly in deep tissues, and to kill tumor cells (Deng et al., 2017; Lin et al., 2021).

Traditional imaging methods, with an emission range of around 400-700 nm, have a shallow depth of tissue penetration. In addition, the imaging quality of deep tissues is rather poor in the first near-infrared (NIR-I; 700-900 nm) area. For this reason, recent research has concentrated on developing photosensitizers that emit light in the second near-infrared (NIR-II; 1000-1700 nm) region where biological imaging can achieve a higher penetration depth and spatial-temporal resolution, allowing an improved monitoring quality (He et al., 2018; Hong et al., 2017). When developing an effective photosensitizer for photodynamic therapy, it is important to keep in mind that the structure of the compound must be carefully crafted to have a high photoluminescence quantum yield (PLQY). This concept is necessary to achieve an adequate amount of emission in the desired region of the electromagnetic spectrum. On the other hand, designing photosensitizers may present obstacles, such as the aggregation-induced quenching (ACQ) effect generated by strong intermolecular π-π interactions, which affects the PLQY of PS and, therefore, the tissue penetration effectiveness (Li et al., 2020).

In recent years, aggregation-induced luminogens (AIEgens) that utilize twisted structures to provide strong photoluminescence by reducing intermolecular π-π interactions have garnered great interest in an effort to prevent this phenomenon. For this reason, numerous luminogens with AIE features and several types of fluorophores producing NIR-II emissions, such as quantum dots (QDs), carbon nanotubes, and organic fluorophores, have garnered considerable interest (J. Wang et al., 2021; S. Xu et al., 2020). Due to their designability of physical and optical properties, minimum biotoxicity, in vivo biocompatibility, and biodegradability, organic fluorophores are the best option with the most clinical translation potential (Sun et al., 2022). Consequently, it is advantageous to decrease the band gap value of photosensitizers by increasing the length of π-conjugation in the construction of D-A-D luminogens since a decrease in the HOMO and LUMO gaps results in red-shifted emission, and thus a decrease in the band gap value of photosensitizers. However, this technique for developing organic NIR-II fluorophores is ineffective compared to visible light emitters. Constructing electron donors (D) that enhance the HOMO level and electron acceptors (A) that decrease the LUMO level may thus be explored as an alternate approach. Therefore, most NIR-II AIEgens are created by strengthening donor and acceptor units (Fan et al., 2021; W. Xu et al., 2021). A new NIR-II emitter displaying AIE properties was successfully synthesized in which a triphenylamine unit was employed as an electron donor (D), and a tetraphenylethene unit was used as a molecular rotor, both of which were installed atop a benzobisthiadiazole (BBT) unit functioning as an electron acceptor (A). This particular compound is also often utilized as a building block for NIR dyes (P. Xu et al., 2020).

In this study, we first investigated the ADMET (absorption, distribution, metabolism, excretion, and toxicity) and, accordingly, drug-likeness properties of designated malononitrile derivatives which could potentially be used as photosensitizers, and in the subsequent step, we carried out a comprehensive molecular docking analysis to explore the potential binding sites of D-A *or* D-A-D type luminogens (Figure 1), with two distinct blood proteins; namely bovine serum albumin (BSA), and human serum albumin (HSA), both of which were found to be effective carriers of several pharmaceuticals against preliminary cancer disease. In this scope, our mechanistic process involves the derivatization of a well-known NIR AIEgen (D. Wang et al., 2019) by altering its donor and acceptor fragments in order to enhance selectivity and binding ability with BSA {Protein Database (PDB) ID: 4F5S} and HSA (PDB ID: 4L9Q). Leveraging these findings, dye molecules with the lowest docking scores were chosen to perform molecular dynamics (MD) simulations (D_1-A_1-D_1:BSA and D_1-A_1:HSA complexes, respectively) to calculate root-mean-square deviation (RMSD) and root-mean-square fluctuations (RMSF) values.

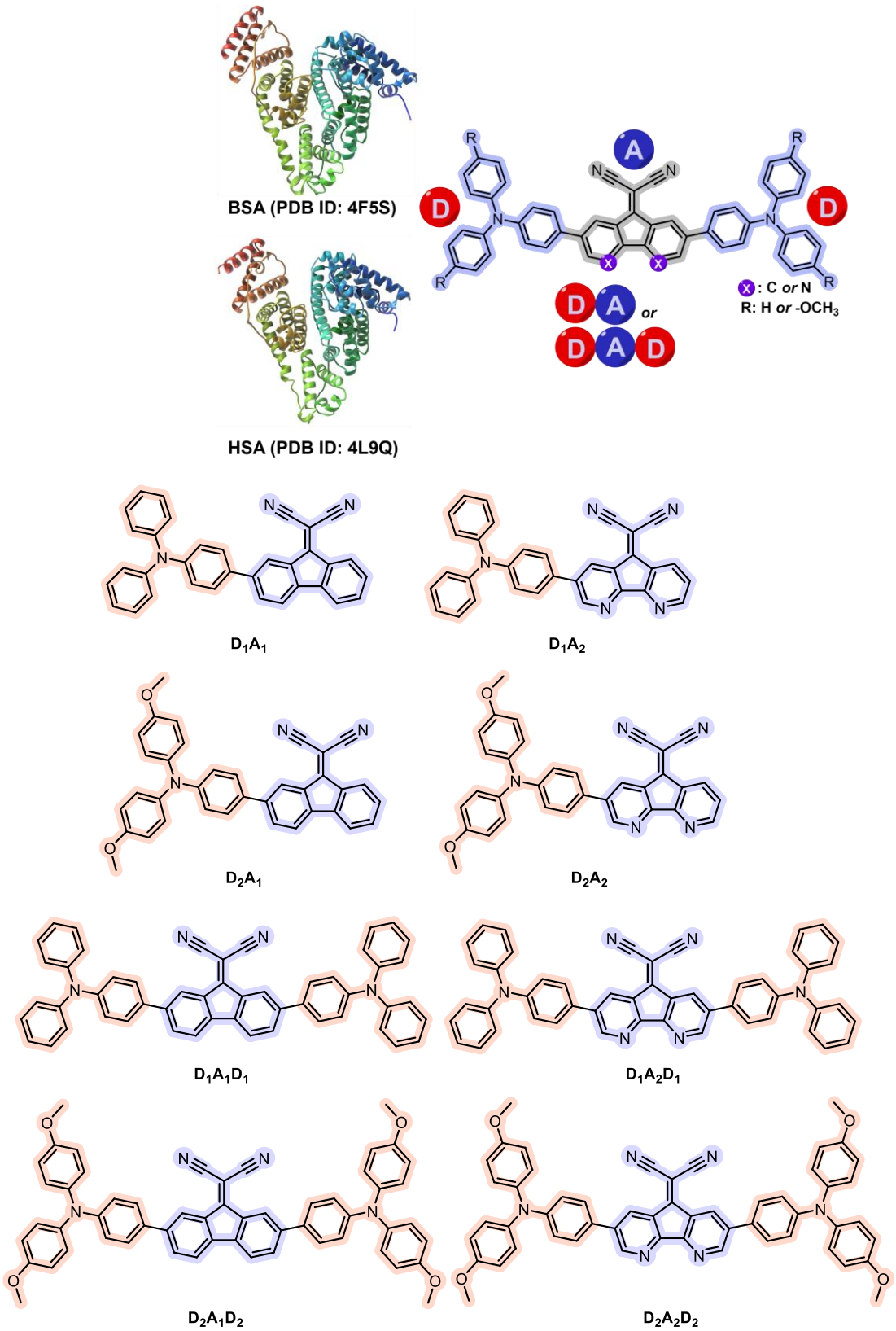

Figure 1. Scope of the investigated D_n-A_n or D_n-A_n-D_n type' AIEgens and serum albumins (HSA and BSA)

2. Materials and Methods

2.1. Density Functional Theory (DFT) Calculations and *In Silico* (ADMET/Drug-likeness) Analyses

2.1.1. Quantum Chemical Calculations

Initial geometries of the target dye molecules to be used for the molecular docking and accordingly, molecular dynamics studies were acquired according to Density Functional Theory (DFT) using Gaussian 09 software (Frisch et al., 2010). To this purpose, D_n-A_n *or* D_n-A_n-D_n backbones were constructed by GaussView (v.5.0.8) (Dennington et al., 2009). Subsequently, the ground-state geometries were predicted *in vacuo* and then the required solvent effects were taken into account implicitly by using the IEPCM of water ($\varepsilon_0 = 80.4$) with B3LYP level of theory and 6-31G(d,p) as the basis set. Following these steps, the local minima were verified, and required vibrational frequency calculations were executed to identify the convergence to a real minimum. Consequently, the absence of imaginary values demonstrated that the geometry optimization processes were completed successfully.

2.1.2. SwissADME Analysis

Numerous ADME analyses have been carried out with the assistance of the online web tool known as SwissADME, which plays a significant role in the determination of several drug-likeness properties of potent drug molecules. These analyses include pharmacokinetic properties, drug-likeness nature, medicinal chemistry friendliness, and bioavailability radar (Daina et al., 2017).

In this study, we computed both Lipinski's rule of five (RO5) parameters such as molecular weight (MW), hydrogen bond acceptor (HBA), hydrogen bond donor (HBD), and consensus logP ($ClogP_{o/w}$), and other descriptive parameters including the number of rotatable bonds (nROTBs), topological polar surface area (TPSA), gastrointestinal absorption (GI abs.), blood-brain barrier (BBB), and solubility (S) of eight potent drug molecules.

The blood-brain barrier, also known as the BBB, is an intricate system of blood arteries and tissue comprised of closely packed cells. Its primary function is to prevent potentially hazardous chemicals from entering the brain (Daneman & Prat, 2015). The BBB was impermeable to all; however, selective for a few tiny particle. This phenomenon might be an issue for therapeutics with a considerable molecular weight that cannot penetrate the blood-brain barrier; as a result, it limits the blood-brain permeability of the molecule and the treatment of a wide variety of brain disorders. In addition, gastrointestinal absorption also depends upon the size of a molecule, and molecules with high molecular weight cannot be absorbed via the gastrointestinal system. For this reason, the molecular weight of a potent pharmaceutical needs to be well below the acceptable range. The molecular weight of a potential therapeutic molecule is predicted to be about 500 g/mol on average (Benet et al., 2016).

Consequently, the number of hydrogen bond acceptors (HBA) and hydrogen bond donors (HBD) is an essential chemical feature for assessing the oral bioavailability of small potential medicines. It is thought that hydrogen bond acceptors and donors are responsible for regulating the process of passive diffusion across cell membranes, which is an essential step in the process of medication absorption and distribution. The optimal HBA and HBD levels are lower than 10 and 5, respectively. In addition, the consensus $logP_{o/w}$ parameter is a coefficient of partition between n-octanol and water, and this descriptor is used to determine the lipophilicity of a pharmacological molecule. Recalling Lipinski's rule of five, the $logP_{o/w}$ value of a potential pharmaceutical must be less than 5 to be sufficiently lipophilic to penetrate the cell membrane. Consensus $logP_{o/w}$ is the average of the five models (iLOGP, XLOGP3, WLOGP, MLOGP, and SILICOS-IT) used to assess the lipophilicity of a pharmaceutical compound (Moriguchi et al., 1994).

In addition, the number of rotatable bonds (nROTBs) is an important measure that indicates the flexibility of a drug molecule, which plays a critical role in the attachment of its macromolecules. It is anticipated that potent medications having a maximum of 9 rotatable bonds (nROTBs) will be sufficiently flexible to attach to their target macromolecule (Daina et al., 2017). In addition, polar surface area (PSA) has been a widely employed molecular descriptor in investigating drug transport properties such as intestinal absorption and BBB penetration. It is the sum of the contributions to the surface area of molecules formed by polar atoms such as oxygen, nitrogen, and their respective hydrogens. Ertl et al. created a quick additive fragment way of computing PSA

for rapid virtual bioavailability screening of a very wide collection of compounds to circumvent complicated PSA computation (Ertl et al., 2000). Since its first publication, the topological polar surface area (TPSA) has gained favor as a virtual screening method in medicinal chemistry. The ideal predicted value of TPSA was determined to be less than 130 $Å^2$. The bioavailability radar map is an additional useful tool for depicting estimated physicochemical data of candidate drug molecules within the context of oral drug-like property space. Several molecular descriptors, including lipophilicity (XLOGP3), size (molecular weight, MW), polarity (TPSA), solubility (logS), saturation, and flexibility (nROTB), whose properties and optimal values have been described above, are used to plot a bioavailability radar consisting of the six parameters as mentioned earlier and the pink hexagonal area representing the acceptable region of these parameters.

2.1.3. Molinspiration Tool

In addition to evaluating the ligands' bioactivity metrics, the drug-likeness of the target molecules was also assessed using Molinspiration, another web-based application that calculates many molecular attributes and the bioactivity score of prospective medications. In this section, we have also intended to estimate the number of Lipinski's rule parameters and other descriptive elements to confirm the SwissADME results of our studied ligands using the Molinspiration tool [Molinspiration Cheminformatics free web services, https://www.molinspiration.com, Slovensky Grob, Slovakia].

2.1.4. OSIRIS Property Explorer

Prediction of activity spectra for substances (PASS) analysis was performed by using OSIRIS Property Explorer (v.4.5.1), which is an online tool that evaluates several pharmacological behaviors and toxicity of candidate drug molecules such as mutagenicity, tumorigenicity, irritation, and reproductive effect [Organic Chemistry Portal. 2012, http://www.organic-chemistry.org/prog/peo/].

2.2. Molecular Docking Studies

DFT-optimized dye molecules were used as inputs for ligand molecules and corresponding docking simulations were carried out using AutoDock Vina (Trott & Olson, 2009) implemented in the SAMSON platform (2022, R2, OneAngstrom). The X-ray crystal structures of bovine serum albumin (PDB ID: 4F5S) and human serum albumin (PDB ID: 4L9Q) were obtained from the Protein Data Bank at www.rcsb.org. After removing water molecules from both macromolecules and extracting the ligand (Teniposide) from HSA, charges and hydrogens were added to the structures of HSA and BSA to be docked. Chain B was deleted from the structures of both HSA and BSA, and Chain A was chosen for the molecular docking procedure. Consecutively, the conformations of ligands with the lowest docked binding energy with BSA (PDB ID: 4F5S) and HSA (PDB ID: 4L9Q) were then selected, and corresponding analysis and visualization of the dye–albumin complexes were performed using both SAMSON and Discovery Studio Visualizer 2021 (client version; Accelrys Software Inc., San Diego, CA, USA).

2.3. Molecular Dynamics Simulations

Molecular dynamics (MD) studies were carried out to investigate the binding stability between the studied ligands, demonstrating the highest docking performances, including D_1-A_1-D_1 and D_1-A_1 with BSA and HSA, respectively. The conformations with the highest binding affinity of D_1-A_1-D_1 and D_1-A_1 structures were obtained from the molecular docking studies, and all the simulations, including the analysis of the trajectories, were carried out with GROningen MAchine for Chemical Simulations (GROMACS) 2021.2 software package by utilizing CHARMM36 force field and TIP3P as the water model. Electrostatic interactions were calculated by Particle Mesh Ewald (PME) method with a Fourier spacing of 0.16 nm and a short-range cut-off of 1.2 nm used for electrostatic treatment. After the addition of Na ions in order to neutralize the system of the complexes, the energy minimization was carried out with the 5000 steps of the steepest descent minimization method until the maximum force was less than 10.0 kJ/mol/nm. Consequently, the system equilibration was performed in two phases consisting of a constant number of particles, volume, and temperature (NVT) and a constant number of particles, pressure, and temperature (NPT). The temperature was increased within 100 ps in the NVT ensemble and kept constant at 299.8 K with the Berendsen Thermostat, followed by the NPT ensemble at 1 bar for 100 ps. 20 ns MD simulation was carried out for both D_1-A_1-D_1:BSA and D_1-A_1:HSA complexes. 2D

plots depicting the root-mean-square deviation (RMSD) and root-mean-square fluctuations (RMSF) which describe the inherent dynamical stabilities of the complexes, were generated.

3. Results and Discussion

3.1. Prediction of ADMET and Drug-likeness Characteristics

3.1.1. SwissADME Analysis

SwissADME findings that were utilized to assess various pharmacokinetic parameters (Table 1) of the potential therapeutic compounds have revealed that our ligands' molecular weight (MW) varied from 471.55 kcal/mol to 836.93 kcal/mol. Amongst the whole ligands, the D_1-A_1 (471.55 g/mol) and D_1-A_2 (473.53 g/mol) were detected within the intended range. The potent drugs' MW data showed low gastrointestinal absorption (GI abs.) and no blood-brain barrier (BBB) permeability. In the ideal range, we also identified HBA values ranging from 2 to 8 and HBD values of 0 for all studied therapeutic molecules. Except for the models D_2-A_1-D_2 and D_2-A_2-D_2, whose values were 12, nROTBs had ideal values ranging between 4 and 8. The TPSA values, which ranged from 50.82 to 116.76 Å^2, were likewise found to be within the permissible range. In addition, the Clog$P_{o/w}$ method utilized to assess the lipophilicity and ranged from 5.22 to 10.27. D_1-A_2 and D_2-A_2 exhibited virtually excellent lipophilic properties with respective values of 5.23 and 5.22. D_n-A_n series were discovered to be weakly soluble in water, while the D_n-A_n-D_n series were found insoluble. Consequently, the SwissADME analysis demonstrated that D_1-A_2, which has no Lipinski violation, is the best potential luminogen among investigated molecules.

Table 1
ADME prediction of the studied ligands (software: SwissADME)

Ligands	MW[a]	HBA[b]	HBD[c]	nROTB[d]	TPSA[e]	GI abs.[f]	BBB[g]	CLog $P_{o/w}$[h]	Solubility[i]	Violation
D_1-A_1	471.55	2	0	4	50.82	Low	No	6.69	PS	1
D_1-A_2	473.53	4	0	4	76.60	Low	No	5.23	PS	0
D_2-A_1	531.60	4	0	6	69.28	Low	No	6.66	PS	2
D_2-A_2	533.58	6	0	6	95.06	Low	No	5.22	PS	1
D_1-A_1-D_1	714.85	2	0	8	54.06	Low	No	10.27	Ins	2
D_1-A_2-D_1	716.83	4	0	8	79.84	Low	No	8.83	Ins	2
D_2-A_1-D_2	834.96	6	0	12	90.98	Low	No	10.24	Ins	2
D_2-A_2-D_2	836.93	8	0	12	116.76	Low	No	8.84	Ins	2

Rules: [a]MW≤500 g/mol, [b]HBA≤10, [c]HBD≤5, [d]nROTB≤9, 20≤[e]TPSA≤130Å^2
Abbreviations: [f]GI abs: Gastrointestinal absorption, [g]BBB: Blood brain barrier, CLog$P_{o/w}$: Consensus log$P_{o/w}$ [i]S: Solubility: PS: Partially soluble, Ins: Insoluble

The bioavailability radar, whose pink hexagonal region symbolizes the optimal drug-likeness of a notorious drug molecule. As shown in Figure 2, it may also be used to describe the pharmacological similarity of D_1-A_2. The radar plot representations of the remaining studied ligands were made available in supplemental electronic material (ESI†). According to the bioavailability radar of D_1-A_2, the lipophilicity and solubility have slightly beyond the target zone. On the other hand, size, polarity, and flexibility were determined to be within the pink hexagonal area. In contrast to these values, it was noticed that the saturation property of D_1-A_2 was a considerable distance away from the ideal zone. The researched potent therapeutic molecule was not judged to be orally bioavailable since it deviated from the permitted limit regarding lipophilicity, solubility, and saturation.

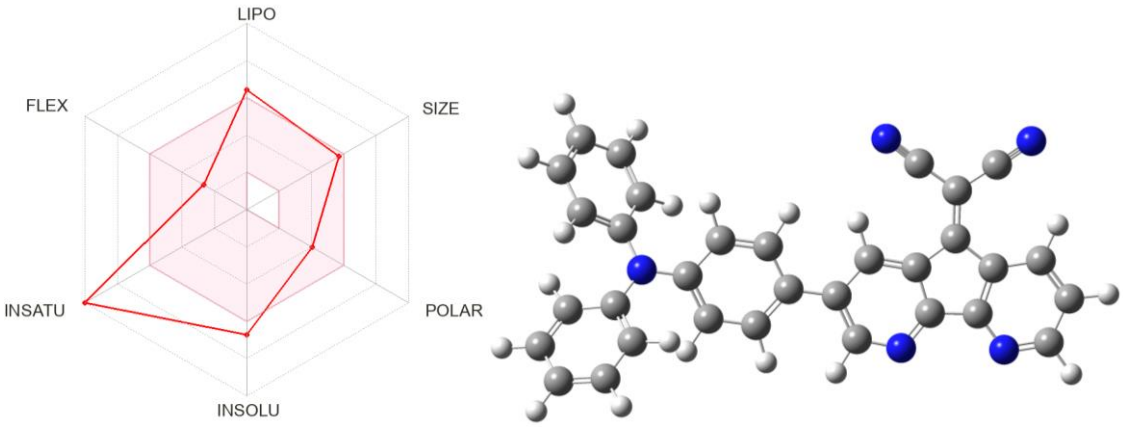

Figure 2. (*left*) Representative bioavailability radar and geometry (*right*) Optimized structure of D_1-A_2.

3.1.2. Molinspiration Tool

Using the Molinspiration tool, the parameters of Lipinski's rule and other descriptive properties were also calculated. Several drug-likeness parameters, such as TPSA, nOHNH (HBD), and nROTB, yielded the same results as the SwissADME report, and miLogP, an additional method for evaluating the lipophilicity characteristics of a ligand, demonstrated that the investigated potent drugs exceeded the optimal range, indicating that these ligands were highly lipophilic. The number of hydrogen bond acceptor (nON) data of the ligands ranged from 3 to 10 and were detected in the acceptable limit, except for D_2-A_2-D_2, which possesses 10 nONs. In this scope, D_1-A_1 and D_1-A_2 showed relatively ideal drug-likeness characteristics, both of which possessed 1 Lipinski Violation.

Table 2
Drug-likeness data of the studied ligands (software: Molinspiration)

Ligands	miLogP[a]	TPSA[b]	nAtoms[c]	nON[d] (HBA)	nOHNH[e] (HBD)	Violation	nROTB[f]	Volume
D_1-A_1	8.61	50.82	37	3	0	1	4	432.76
D_1-A_2	7.21	76.61	37	5	0	1	4	424.44
D_2-A_1	8.67	69.29	41	5	0	2	6	483.85
D_2-A_2	7.32	95.07	41	7	0	2	6	475.53
D_1-A_1-D_1	9.96	54.06	56	4	0	2	8	659.77
D_1-A_2-D_1	9.73	79.84	56	6	0	2	8	651.45
D_2-A_1-D_2	9.99	91.00	64	8	0	2	12	761.95
D_2-A_2-D_2	9.77	116.8	64	10	0	2	12	753.64

Abbreviations: [a]miLogP: Partition coefficient between n-octanol and water ($logP_{o/w}$), [b]TPSA: Topological polar surface area, [c]nAtoms: Number of atoms, [d]nON: Number of hydrogen bond acceptors (HBA), [e]nOHNH: Number of hydrogen bond donors (HBD), [f]nROTB: Number of rotatable bonds

G protein-coupled receptor ligands, also known as GPCRs, are members of a large family of signaling proteins responsible for mediating cells' responses to a wide variety of hormones, metabolites, cytokines, and neurotransmitters. About 800 genes are contained within this receptor family, and they are responsible for regulating a wide array of signaling pathways related to behavior, blood pressure control, cognition, immune response, mood, and taste. Due to their high susceptibility to inhibition by pharmacological agents, GPCRs are ideal targets for the research and development of new drugs (Basith et al., 2018). Table 2 summarizes the results for the bioactivity descriptors GPCR Ligands (GPCRL), Ion Channel Modulator (ICM), Nuclear Receptor Ligand (NRL), Protease Inhibitor (PI), and Enzyme Inhibitor (EI) that are evaluated as part of the Molinspiration service. In terms of bioactivity scores, it should be noted that values greater than 0.0 display significant bioactivity, while values ranging from -0.50 to 0.0 show moderate activity, and bioactivity score value less than -0.50 are classified as inactive. As a result, according to the data, D_n-A_n type dyes have shown relatively ideal bioactivity, especially when compared with the D_n-A_n-D_n. Considering the GPCRL grades displayed in Table 3 for each of the photosensitizers we researched, the D_n-A_n series of luminogens possess relatively higher scores ranging from -0.08 to -0.02, and as a result, these ligands have moderate bioactivity. D_n-A_n-D_n series of luminogens, on the other hand, were found to be below the lowermost limit of the bioactivity, which ranged from -3.18 to -1.59. In addition, ion channels are the fundamental mechanism behind the vast majority of

physiological processes. These processes include rapid cell misconfigurations, the contraction of cardiac and skeletal muscles, neuronal activity, the transport of nutrients and ions across epithelial membranes, hormone production, the immune response, and the proliferation of tumor cells. Furthermore, ion channels are the basis of the vast majority of physiological processes, including rapid cell misconfigurations, cardiac and muscular contraction, neuronal activity, epithelial transport of nutrients and ions, hormone production, immunological response, and tumor cell proliferation. It is no surprise that ion channels are also considered a popular therapeutic target for drug developers. ICM scores of our investigated luminogens demonstrate that the D_n-A_n series also had relatively higher scores, ranging from -0.54 to -0.16, compared to the D_n-A_n type of luminogens, which diverged from -3.65 to -2.76.

Table 3
Bioactivity scores of the studied ligands (software: Molinspiration)

Ligands	GPCRL	ICM	KI	NRL	PI	EI
D_1-A_1	-0.03	-0.28	-0.03	-0.14	-0.02	-0.06
D_1-A_2	-0.02	-0.16	0.17	-0.20	0.04	0.01
D_2-A_1	-0.08	-0.54	-0.15	-0.25	-0.06	-0.20
D_2-A_2	-0.07	-0.44	0.02	-0.30	-0.01	-0.14
D_1-A_1-D_1	-1.59	-2.83	-2.23	-2.42	-1.10	-2.05
D_1-A_2-D_1	-1.60	-2.76	-2.12	-2.45	-1.07	-2.02
D_2-A_1-D_2	-3.17	-3.65	-3.55	-3.59	-2.63	-3.46
D_2-A_2-D_2	-3.18	-3.63	-3.51	-3.60	-2.61	-3.44

Abbreviations: GPCRL: G protein-coupled receptor ligands, ICM: Ion Channel Modulator, KI: Kinase Inhibitor, NRL: Nuclear Receptor Ligand, PI: Protease Inhibitor, EI: Enzyme Inhibitor

Moreover, kinases have been extensively studied as therapeutic targets, and deregulation of kinase function has been shown to play a role in immunological, inflammatory, degenerative, metabolic, cardiovascular, and viral illnesses, in addition to cancer. Thus, kinases are appealing targets due to their demonstrated druggability and clinical safety profile of authorized kinase inhibitors. When we consider our findings for KI, we may observe that scores of our ligands varied from -3.55 to 0.02, showing that the D_n-A_n series were more prominent than D_n-A_n-D_n luminogens once more. It should be noted that these series were also found to have higher bioactivity score in comparison with D_n-A_n-D_n type photosensitizers in terms of NRL, PI, and EI calculations, and the value of each parameter was considered to demonstrate moderate bioactivity characteristics. More specifically, nuclear receptor ligands, also known as NRLs, are ligand-inducible transcription factors that directly influence gene transcription after translocating to the nucleus. They have an important role in essential physiological processes, such as cell proliferation, development, immunity, metabolism, and reproduction, which significantly impact the process of developing new drugs, according to the data in **Table 3.** NRL scores of our ligands diverged from -3.60 to -0.14. In the cases of Protease Inhibitor (PI) parameter and Enzyme Inhibitor (EI) factor, the results varied from -2.63 to 0.04 and -3.46 to 0.01, respectively. As mentioned above, bioactivity scores of the D_n-A_n series gave higher results than the rest of our investigated luminogens, indicating that these series have moderate bioactivity.

3.1.3. OSIRIS Property Explorer

In addition to Lipinski's rule of five (RO5) evaluation, the drug-likeness and drug score of our examined ligands were also calculated by OSIRIS Property Explorer, as were several toxicity risk factors, including mutagenicity, tumorigenicity, skin irritation, and reproductive impact parameters. The provided data in Table 4 shows that the cLogP and water solubility characteristics are inversely proportional. It is well known that our molecules are strongly lipophilic, which results in a solubility in water that is significantly lower than average. cLogP values varied from 5.58 to 11.79, while negative results were observed for the solubility of our ligands, which ranged from -17.67 to -9.20. TPSA has also provided the same results with Molinspiration and SwissADME reports. In light of the OSIRIS Property Explorer calculations, the drug-score data demonstrated notable differences among the ligands under investigation. Importantly, the drug-score values for D_1-A_2 (0.13) and D_2-A_2 (0.12) were significantly higher compared to those of the other ligands in the series. While these drug-scores might not be considered exceptional, it is crucial to interpret them in relation to the entire series of ligands, as well as in the context of their specific application in photodynamic therapy. Consequently, D_1-A_2 and D_2-A_2 exhibit relatively better druggability potential within this series of newly designed dye molecules.

Table 4
Drug-likeness properties of the studied ligands (software: OSIRIS)

Ligands	cLogp	Solubility	MW	TPSA	Drug-likeness	Drug-score
D_1-A_1	7.54	-11.40	471	50.82	-10.58	0.02
D_1-A_2	5.72	-9.20	473	76.60	-10.50	0.13
D_2-A_1	7.40	-11.45	531	69.28	-8.95	0.02
D_2-A_2	5.58	-9.24	533	95.00	-8.95	0.12
D_1-A_1-D_1	11.79	-17.67	714	54.06	-10.39	0.01
D_1-A_2-D_1	9.97	-15.47	716	79.84	-10.63	0.07
D_2-A_1-D_2	11.51	-17.74	834	90.94	-8.82	0.01
D_2-A_2-D_2	9.69	-15.54	836	116.70	-9.08	0.06

In terms of toxicity, D_1-A_1 and D_2-A_1 displayed considerably high mutagenic, tumorigenic, and compelling reproductive features, but the other investigated ligands did not demonstrate any of these types of toxicity (Table 5). In addition, OSIRIS has determined that D_1-A_1-D_1 and D_2-A_1-D_2 exhibited severe skin irritation characteristics, which is another disadvantage for a therapeutic molecule in the development stage. Consequently, D_1-A_2, D_2-A_2, D_1-A_2-D_1, and D_1-A_2-D_1 did not produce any of the types mentioned above of toxicity properties; hence, these studied ligands could be allowed to be evaluated as potentially effective therapeutic drugs for PDT.

Table 5
Toxicity results of the investigated luminogens (software: OSIRIS)

Ligands	Mutagenic	Tumorigenic	Irritant	Reproductive Effective
D_1-A_1	🔴	🔴	🟢	🔴
D_1-A_2	🟢	🟢	🟢	🟢
D_2-A_1	🔴	🔴	🟢	🔴
D_2-A_2	🟢	🟢	🟢	🟢
D_1-A_1-D_1	🟢	🟢	🔴	🟢
D_1-A_2-D_1	🟢	🟢	🟢	🟢
D_2-A_1-D_2	🟢	🟢	🔴	🟢
D_2-A_2-D_2	🟢	🟢	🟢	🟢

🟢 : no detectable toxicity 🔴 : potent toxicity

3.2. Molecular Docking Studies

In this study, we carried out an extensive molecular docking strategy to become familiar with the binding affinities of donor-acceptor-donor (D-A-D) and donor-acceptor (D-A) types of AIE luminogens with blood proteins. More specifically, we focused on bovine serum albumin (BSA) and human serum albumin (HSA), both of which have shown promise as reliable carriers of a wide range of pharmaceuticals against cancer and infectious disorders in the early stages. For the aim of this study, a molecular docking simulation was carried out between eight prospective drug molecules and the above-described blood proteins. Docking scores and domain interactions of the ligand and albumin complexes have been listed in Table 6.

Table 6
Docking scores and binding domains of the investigated ligands with BSA and HSA

Structure and Active Sites of BSA and HSA

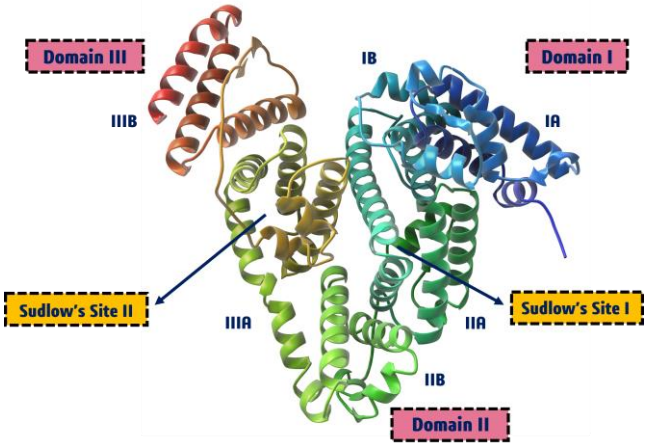

Docking Scores and Binding Domains of Ligand and Protein Complexes

Ligands	Binding scores		Binding domains	
	BSA	HSA	BSA	HSA
D_1-A_1	-9.10	-10.50	IB	IB
D_1-A_2	-11.40	-9.90	IA & IB	IB
D_2-A_1	-8.90	-10.00	IB & IIIA	IB
D_2-A_2	-8.50	-9.40	IB	IB & IIIA
D_1-A_1-D_1	-11.70	-10.10	IA & IB & IIIA	IB
D_1-A_2-D_1	-10.90	-9.70	IB & IIIA	IB
D_2-A_1-D_2	-8.80	-8.80	IB & IIIA & IIIB	IB
D_2-A_2-D_2	-8.50	-8.40	IB & IIIA & IIIB	IB & IIIA

As can be seen from the inner figure of Table 6, BSA and HSA proteins, which have an amino acid sequence identity of 75.52%, consist of three main domains, including Domain I, Domain II, and Domain III, and each of these domains contains two sub-domains such as IA, IB, IIA, IIB, IIIA, and IIIB (Akdogan et al., 2012). The primary regions of ligand binding sites in BSA and HSA are located in hydrophobic voids in subdomains IIA and IIIA, also known as Sudlow's site I and Sudlow's site II, respectively, according to crystal structural investigations. These ligand-binding sites can be found in both BSA and HSA. When the data from the binding domains of the proteins and complexes we studied are considered, it is possible to conclude that most of our luminogens bind to more than one sub-domain. More specifically, in the complexes formed between the ligands and BSA, D_1-A_1 possesses the highest docking score, and D_2-A_2 bonded to the IB sub-domain while D_2-A_1 and D_1-A_2-D_1 interacted with IB & IIIA sub-domains. D_2-A_1-D_2 and D_2-A_2-D_2 interacted with similar regions of BSA and bonded to IB, IIIA, and IIIB sub-domains. Additionally, D_1-A_2 and D_1-A_1-D_1 bonded to IA and IB; IA, IB, and IIIA sub-domains, respectively. In the case of the ligand and HSA interactions, the majority of our prospective molecules, including D_1-A_1, D_1-A_2, D_2-A_1, D_1-A_1-D_1, D_1-A_2-D_1, D_2-A_1-D_2 bonded to IB sub-domain. Moreover, the remaining ligands; such as D_1-A_1 and D_2-A_2-D_2, interacted with the IB and IIIA sub-domains of HSA (Figure 3 and Figure S3-S4).

Binding scores of the D_n-A_n series with BSA varied from -8.50 to -11.40 kcal/mol, whereas the D_n-A_n-D_n series ranged between -8.50 to -11.70 kcal/mol. It is essential to point out that D_1-A_1-D_1 possessed the most efficient interaction with BSA, as measured by its binding score, which was determined to be -11.70 kcal/mol. It has provided a result that is far greater than the rest of our potent photosensitizers. When the structure of D_1-A_1 was examined, it should be emphasized that the triphenylamine ring served as a donor (D_1) unit along with 2-

(9H-fluoren-9-ylidene) malononitrile played the role of acceptor (A_1) fragment. It is also possible to claim that the decreasing order of the binding efficiency of our previously studied luminogens that have binding contact with BSA is as follows: D_1-A_1-D_1 (-11.70 kcal/mol) > D_1-A_2 (-11.40 kcal/mol) > D_1-A_2-D_1 (-10.90 kcal/mol) > D_1-A_1 (-9.10 kcal/mol) > D_2-A_1 (-8.90 kcal/mol) > D_2-A_1-D_2 (-8.80 kcal/mol) > D_2-A_2 (-8.50 kcal/mol) = D_2-A_2-D_2 (-8.50 kcal/mol). On the other hand, when ligands and HSA interactions were considered, the docking scores of the D_n-A_n series possessed a scale of -9.40 to -10.50 kcal/mol, while those of D_n-A_n-D_n series ranged from -8.40 to -10.10 kcal/mol. D_1-A_1 has delivered the best binding efficiency with HSA, which has a docking score of -10.50 kcal/mol. At the same time, the binding efficiency of our studied luminogens that have binding interaction with BSA could be ranked in decreasing order as follows: D_1-A_1 (-10.50 kcal/mol) > D_1-A_1-D_1 (-10.10 kcal/mol) > D_2-A_1 (-10.00 kcal/mol) > D_1-A_2 (-9.90 kcal/mol) > D_1-A_2-D_1 (-9.70 kcal/mol) > D_2-A_2 (-9.40 kcal/mol) > D_2-A_1-D_2 (-8.80 kcal/mol) > D_2-A_2-D_2 (-8.40 kcal/mol). In addition, we have also investigated the interactions that take place between the ligands and the amino acid residues present in BSA and HSA. The data on residue interactions for D_1-A_1 were listed in Table 7, and the data on the remainder of our analyzed ligand and residue interactions could be found in the electronic supplementary material (ESI†). For D_1-A_1-D_1 and residue interactions of BSA, hydrogen bonding interactions with GLN33, hydrogen bonding, hydrophobic and electrostatic interactions with LYS204, and hydrophobic interactions including TYR84, HIS105 and LYS465 have been observed. For D_1-A_1 and residue interactions of HSA, on the other hand, D_1-A_1 was surrounded by ARG185, ALA125, ILE141, LEU114, LEU181, and LYS136, and only hydrophobic interactions were observed between the ligand and the residues.

Table 7
Interactions of D_1-A_1-D_1 and D_1-A_1 with serum albumins (BSA and HSA, respectively)

D_1-A_1-D_1 with BSA			
Distance	**Category**	**Type of Interactions**	**Residue Information**
3.02	HB; E	Pi-Ca; Pi-Do HB	LYS204
3.20	HB	Pi-Do HB	GLN33
4.94	Other	Pi-S	MET87
4.90	Hyd	Pi-Pi-T-Sh	TYR84
5.21	Hyd	Pi-Pi-T-Sh	HIS105
4.59	Hyd	Pi-Al	LYS465
4.84	Hyd	Pi-Al	LYS465
4.85	Hyd	Pi-Al	LYS204
D_1-A_1 with HSA			
Distance	**Category**	**Type of Interactions**	**Residue Information**
2.70	Hyd	Pi-Sg	LYS136
4.20	Hyd	Pi-Al	LYS136
4.60	Hyd	Pi-Al	ALA125
4.70	Hyd	Pi-Al	LYS136
5.03	Hyd	Pi-Al	LEU114
4.70	Hyd	Pi-Al	LEU114

D_1-A_1-D_1:BSA (PDB ID: 4F5S)

Binding score: -11.70 kcal/mol || Binding domain: IA & IB & IIIA

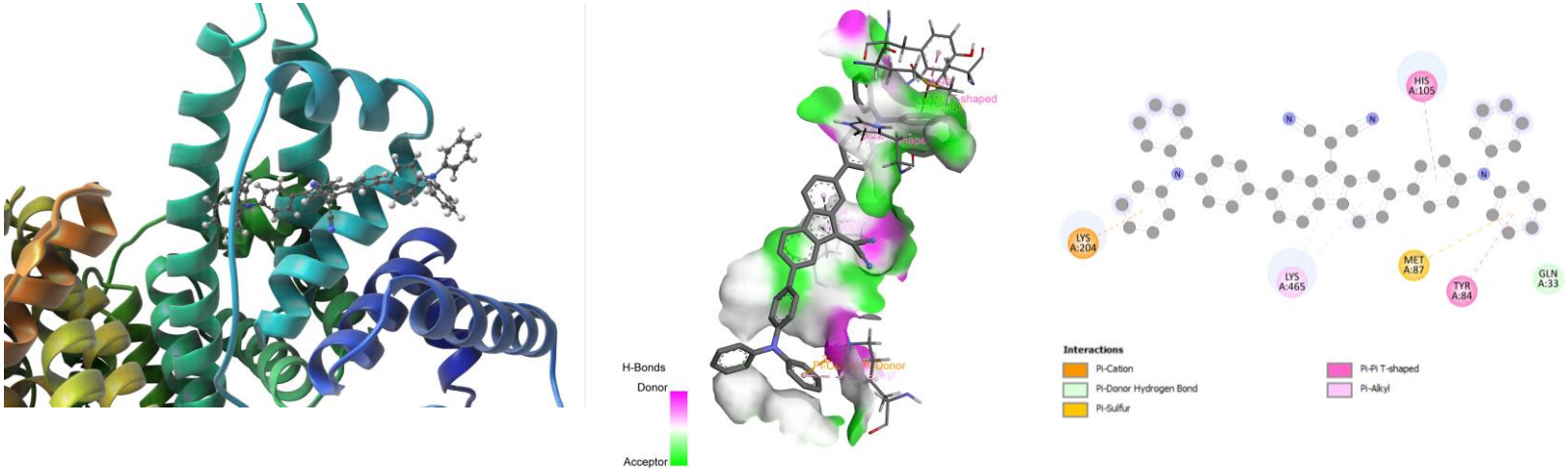

D_1-A_1:HSA (PDB ID: 4L9Q)

Binding score: -10.50 kcal/mol || Binding domain: IB

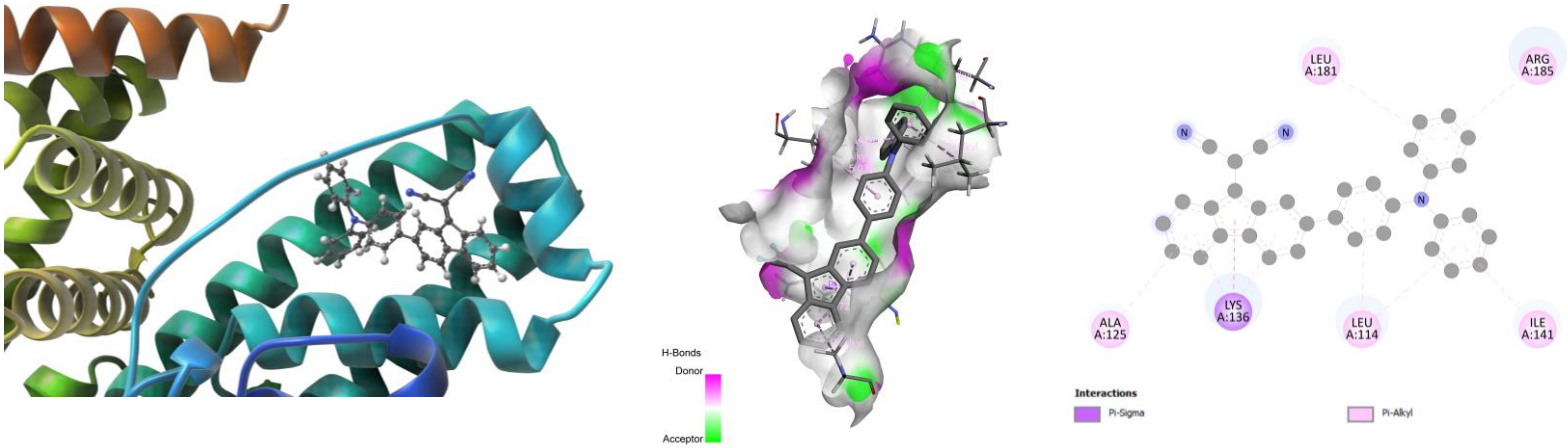

Figure 3. Binding poses and residue interactions of D_1-A_1-D_1:BSA and D_1-A_1:HSA

3.3. Molecular Dynamics Simulations

In order to determine the equilibrium statement of the best docked ligands (D_1-A_1, D_1-A_1-D_1) and D_1-A_2 possessing the highest drug-score calculated by OSIRIS with the target serum albumins, molecular dynamics simulations were performed for 20 ns to evaluate the impact of structural variations such as the conformational stability, conformational alterations, internal motions, and protein-ligand interactions of the best binding complexes (Islam et al., 2020).

3.3.1. Root Mean Square Deviation (RMSD) Analysis

Root mean square deviation (RMSD) plot of a resulting MD trajectory generally represents the characterization and the conformational comparison of protein or protein-ligand complexes over a period of time (Akdogan et al., 2012). In addition, the structural stability of protein-ligand complexes could also be evaluated and analysed by RMSD plots, which is conveniently calculated using the GROMACS software package.

RMSD calculation is based mathematically on the following equation (3.1);

$$RMSD = \sqrt{\frac{\sum_{i=1}^{N} m_i (r_i - r_i^0)^2}{\sum_{i=1}^{N} m_i}} \quad (3.1)$$

where m_i represents the mass of atom i, r_i and r_i^0 are represented as the coordination of atom i at any distance during MD analysis and its reference state, respectively (Ajloo et al., 2013).

Molecular dynamics simulations were carried out at 300 and 310K for complexes with the highest binding affinities, specifically D_1-A_1-D_1:BSA and D_1-A_1:HSA. Additionally, due to its relatively higher drug-score as assessed by the OSIRIS platform, the D_1-A_2:BSA complex was also studied, as the ligand exhibited a higher docking score with BSA. The resulting RMSD graph is presented in Figure 4.

Upon evaluation of these analyses, the D_1-A_1-D_1:BSA complex displayed an average RMSD value of 0.28 nm, with minor fluctuations occurring between the 7th-9th, 12th-14th, and 17th-19th ns before reaching equilibrium. The complex simulated at 310K exhibited an RMSD value of 0.32 nm, with a noticeable trough around the 4th and 5th ns and a minor peak in the 10th-12th ns range, followed by equilibrium attainment with some fluctuations throughout the remaining time frame.

Conversely, as mentioned earlier, the OSIRIS platform highlighted the substantial druglikeness of D_1-A_2 with a drug-score value of 0.13. In the molecular docking results, this ligand demonstrated a stronger binding score with BSA. Consequently, molecular dynamics simulations of D_1-A_2 with BSA were performed at both 300 and 310K to determine their dynamic behavior within the serum albumin protein. The molecular dynamics results of these complexes were evaluated through corresponding RMSD plots displayed in Figure 4.

The RMSD graphs of D_1-A_2:BSA complexes at 300 and 310K revealed average RMSD values of approximately 0.25 nm and 0.47 nm, respectively. The 300K-associated complex system remained stable during the first 6 ns, followed by an increasing trend throughout the remainder of the trajectory. This trajectory concluded with minor fluctuations between the 12th and 20th ns. For the complex with MD simulation conducted at 310K, the trajectory exhibited sharp peaks and fluctuations until a significant peak was detected at the 8th ns, after which the system equilibrated throughout the remaining time frame.

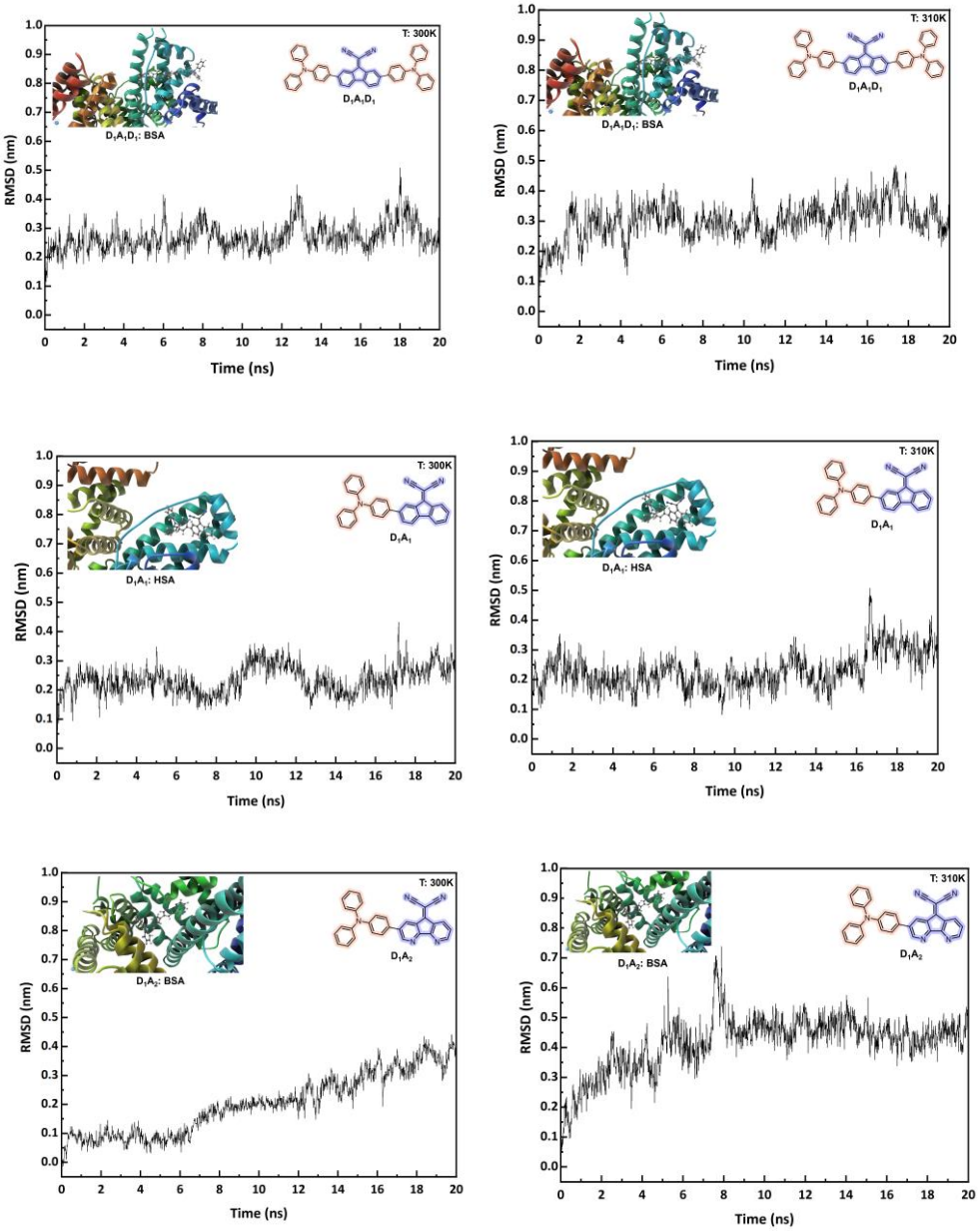

Figure 4. Comparative RMSD trajectory plots of D_1-A_1-D_1:BSA, D_1-A_1:HSA and D_1-A_2:BSA at different temperatures (300 and 310K)

3.3.2. Root Mean Square Fluctuation (RMSF) Analysis

The Root Mean Square Fluctuation (RMSF) is a statistical tool utilized to examine variations in the locations of ligand atoms and changes in the local environment of the protein chain residues at a specific temperature and pressure (Avti et al., 2021; Surti et al., 2020). Since the RMSF (root-mean-square fluctuation) helps to comprehend the area of protein that is being fluctuated throughout the simulation, the flexibility of each residue is estimated to obtain a better understanding of the amount to which the binding of ligand influences the protein's ability to be flexible. RMSF calculation could also be mathematically defined in the following equation (3.2);

$$RMSF = \sqrt{\frac{1}{N}\sum_j^N \left(x_{i(j)} - \langle x_i \rangle\right)^2} \quad (3.2)$$

where $x_{i(j)}$ represents the location (coordinates) of the i^{th} C atom in the structure of the j^{th} model, and x_i is the average position of the i^{th} C atom in all models generated by this approach (Mishra et al., 2021).

Figure 5 presents the RMSF values for each complex system, including D_1-A_1-D_1:BSA, D_1-A_1:HSA, and D_1-A_2:BSA at 300K and 310K, which indicate the adaptability of the ligand within the receptor network and the mobility of residues within the protein. A rigid protein secondary structure characterized by bends, coils, and twists suggests a flexible complex with fewer fluctuations, achieved by permitting a lower RMSF value, while a higher value denotes a more loosely bonded structure (Lokhande et al., 2022). To ascertain the average position of each residue, the RMSF of Cα atoms was applied to the entire protein structure and the ligand. The Cα-RMSF graphs of both D_1-A_1-D_1:BSA and D_1-A_1:HSA complexes, with molecular dynamics simulations completed at 300K, are depicted in Figure 5. The average RMSF values for D_1-A_1-D_1:BSA were found to be 0.15 nm, while those for D_1-A_1:HSA were 0.16 nm. Both graphs exhibited significant peaks around residue number 300 and several peaks between 500 and 600. For the corresponding complexes also simulated at 310K, the average RMSF values of D_1-A_1-D_1:BSA and D_1-A_1:HSA were determined to be 0.16 nm, indicating similar interaction strengths at the specified temperatures. These results suggest that our models, including D_1-A_1-D_1 and D_1-A_1, exhibit comparable characteristics in terms of interaction strength with the amino acids of the respective proteins tested at both 300K and 310K. Regarding the D_1-A_2:BSA complex, with RMSF calculated at 300K and 310K, the ligand displayed a more intimate interaction strength, as evidenced by the RMSF of this complex at 300K, having an average value of 0.18 nm, while this value was determined to be 0.19 nm at 310K.

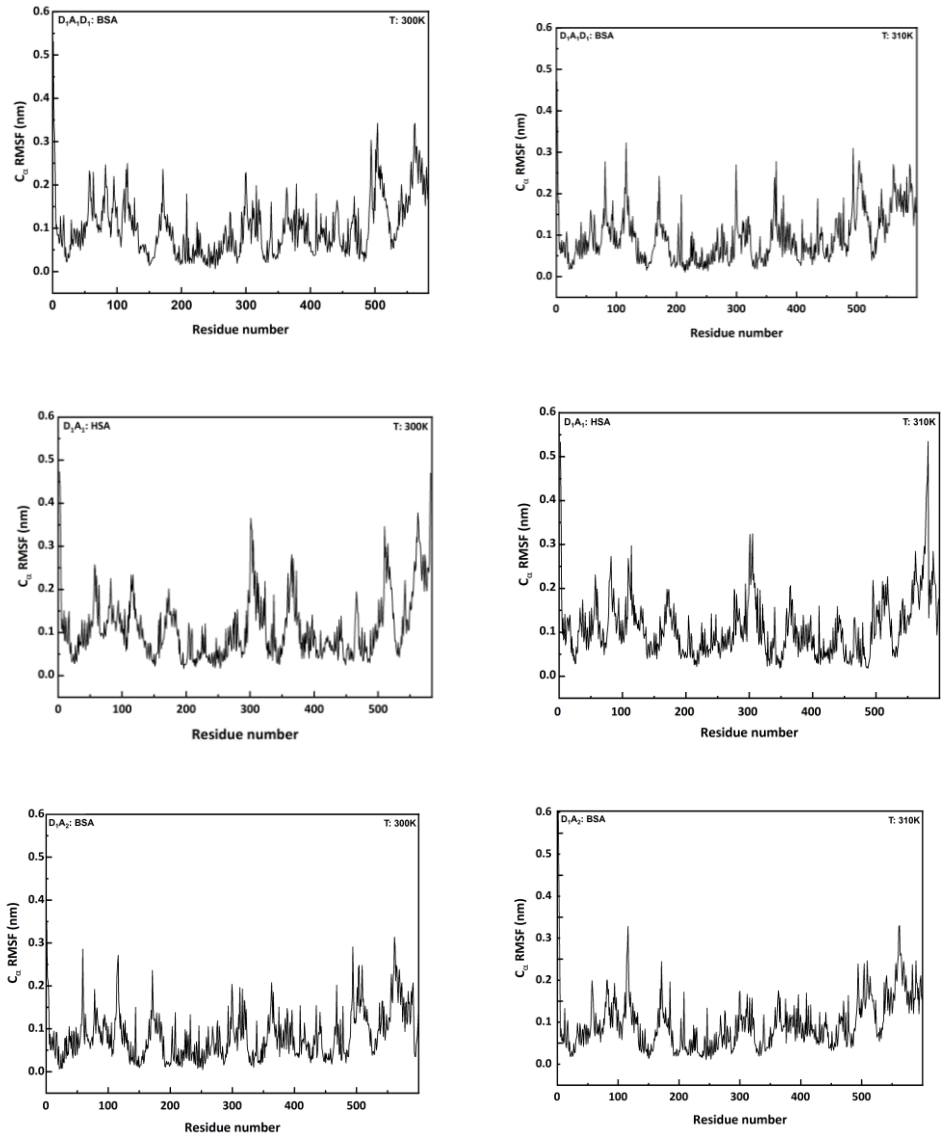

Figure 5. C_α RMSF trajectory plots of (*left, a*) D_1-A_1-D_1:BSA and (*right, b*) D_1-A_1:HSA

4. Conclusion

This study aimed to disclose the pharmacokinetic properties of newly tailored organic NIR-AIEgens as potent fluorescence imaging (FLI)-based photodynamic cancer therapy (PDT) agents and investigate their binding ability to two blood proteins, HSA and BSA. According to SwissADME analysis, D_1-A_2, which has no Lipinski violation, was found the best potential luminogen among the investigated molecules. On the other hand, following Molinspiration outputs, D_1-A_1 and D_1-A_2 dye molecules showed relatively ideal drug-likeness characteristics, which possessed only one Lipinski violation. Furthermore, according to OSIRIS Property Explorer calculation, the drug-score data revealed the distinctive properties among the ligands, and the drug-scores of D_1-A_2 (0.13) and D_2-A_2 (0.12) were found to be significantly higher than those of the other ligands in the series; as a result, these two models were found prominent in terms of druggability. The toxicity results of D_1-A_2 and D_2-A_2 demonstrated no toxicity indications. In addition, we also performed a detailed molecular docking analysis, and D_1-A_1-D_1 exhibited the best binding performance (-11.70 kcal/mol) with BSA by binding its IA, IB, and IIIA sub-domains. On the other hand, D_1-A_1 displayed the highest docking score with HSA (-10.50 kcal/mol) and bonded to its IB sub-domain. We also performed molecular dynamics simulation for the ligands with the top binding affinities to HSA and BSA to reveal the conformational alterations. Considering the predicted RMSD values, we found that the D_1-A_1:HSA complex has a greater degree of stability than the D_1-A_1-D_1:BSA complex. It was also possible to deduce, based on the RMSF trajectories of both systems, that whereas D_1-A_1-D_1:BSA (avg. 0.15 nm) showed slight fluctuations in comparison to D_1-A_1:HSA (avg. 0.16 nm) and it could be seen that the D_1-A_1-D_1:BSA complex demonstrated slightly more flexibility according to the RMSF plot. In light of these findings, we expect that our candidate NIR AIEgens employed in this work will give a valuable theoretical viewpoint for future research in the field of PDT.

Acknowledgement

The authors acknowledge TUBITAK/ULAKBIM (High Performance and Grid Computing Center: TRUBA) to provide computational facilities.

Author Contributions

Harun Nalçakan: performed theoretical calculations and wrote the paper.
Gülbin Kurtay: conceived/supervised the study and wrote the paper.

Conflicts of Interest

The authors declare no conflict of interest.

References

Ajloo, D., Fazeli, S. M., & Amirani, F. J. (2013). Interaction of Cationic and Anionic Phthalocyanines with Adenosine Deaminase, Molecular Dynamics Simulation and Docking Studies. *Computational Molecular Bioscience*, *03*(04), 81–93. https://doi.org/10.4236/cmb.2013.34010

Akdogan, Y., Reichenwallner, J., & Hinderberger, D. (2012). Evidence for Water-Tuned Structural Differences in Proteins: An Approach Emphasizing Variations in Local Hydrophilicity. *PLoS ONE*, *7*(9), e45681. https://doi.org/10.1371/journal.pone.0045681

Avti, P., Chauhan, A., Shekhar, N., Prajapat, M., Sarma, P., Kaur, H., Bhattacharyya, A., Kumar, S., Prakash, A., Sharma, S., & Medhi, B. (2021). Computational basis of SARS-CoV 2 main protease inhibition: an insight from molecular dynamics simulation based findings. *Journal of Biomolecular Structure and Dynamics*, 1–11. https://doi.org/10.1080/07391102.2021.1922310

Benet, L. Z., Hosey, C. M., Ursu, O., & Oprea, T. I. (2016). BDDCS, the Rule of 5 and drugability. *Advanced Drug Delivery Reviews*, *101*, 89–98. https://doi.org/10.1016/j.addr.2016.05.007

Chakraborty, D., Musib, D., Saha, R., Das, A., Raza, M. K., Ramu, V., Chongdar, S., Sarkar, K., & Bhaumik, A. (2022). Highly stable tetradentate phosphonate-based green fluorescent Cu-MOF for anticancer therapy and antibacterial activity. *Materials Today Chemistry*, *24*, 100882. https://doi.org/10.1016/j.mtchem.2022.100882

Chandra, S., Qureshi, S., Chopra, D., Dwivedi, A., & Ray, R. S. (2022). Involvement of Type-I and Type-II Photodynamic Reactions in Photosensitization of Fragrance Ingredient 2-acetonaphthone. *Photochemistry and Photobiology*, *98*(5), 1050–1058. https://doi.org/10.1111/php.13593

Cox, T. R. (2021). The matrix in cancer. *Nature Reviews Cancer*, *21*(4), 217–238. https://doi.org/10.1038/s41568-020-00329-7

Daina, A., Michielin, O., & Zoete, V. (2017). SwissADME: a free web tool to evaluate pharmacokinetics, drug-likeness and medicinal chemistry friendliness of small molecules. *Scientific Reports*, *7*(1), 42717. https://doi.org/10.1038/srep42717

Daneman, R., & Prat, A. (2015). The Blood–Brain Barrier. *Cold Spring Harbor Perspectives in Biology*, *7*(1), a020412. https://doi.org/10.1101/cshperspect.a020412

Debela, D. T., Muzazu, S. G., Heraro, K. D., Ndalama, M. T., Mesele, B. W., Haile, D. C., Kitui, S. K., & Manyazewal, T. (2021). New approaches and procedures for cancer treatment: Current perspectives. *SAGE Open Medicine*, *9*, 205031212110343. https://doi.org/10.1177/20503121211034366

Deng, K., Li, C., Huang, S., Xing, B., Jin, D., Zeng, Q., Hou, Z., & Lin, J. (2017). Recent Progress in Near Infrared Light Triggered Photodynamic Therapy. *Small*, *13*(44), 1702299. https://doi.org/10.1002/smll.201702299

Dennington, R., Keith, T., & Millam, J. (2009). GaussView, Version 5.0.8. *GaussView, Version 5.0.8*.

Dewaele, M., Maes, H., & Agostinis, P. (2010). ROS-mediated mechanisms of autophagy stimulation and their relevance in cancer therapy. *Autophagy*, *6*(7), 838–854. https://doi.org/10.4161/auto.6.7.12113

Ertl, P., Rohde, B., & Selzer, P. (2000). Fast Calculation of Molecular Polar Surface Area as a Sum of Fragment-Based Contributions and Its Application to the Prediction of Drug Transport Properties. *Journal of Medicinal Chemistry*, *43*(20), 3714–3717. https://doi.org/10.1021/jm000942e

Escudero, A., Carrillo-Carrión, C., Castillejos, M. C., Romero-Ben, E., Rosales-Barrios, C., & Khiar, N. (2021). Photodynamic therapy: photosensitizers and nanostructures. *Materials Chemistry Frontiers*, *5*(10), 3788–3812. https://doi.org/10.1039/D0QM00922A

Fan, M., Xu, Z., Liu, M., Jiang, Y., Zheng, X., Yang, C., Law, W.-C., Ying, M., Wang, X., Shao, Y., Swihart, M. T., Xu, G., Yong, K.-T., & Tang, B. Z. (2021). Recent advances of luminogens with aggregation-induced emission in multi-photon theranostics. *Applied Physics Reviews*, *8*(4), 041328. https://doi.org/10.1063/5.0071142

Frisch, M. J., Trucks, G. W., Schlegel, H. B., Scuseria, G. E., Robb, M. A., Cheeseman, J. R., Scalmani, G., Barone, V., Mennucci, B., Petersson, G. A., Nakatsuji, H., Caricato, M., Li, X., Hratchian, H. P., Izmaylov, A. F., Bloino, J., Zheng, G., Sonnenberg, J. L., Hada, M., … Fox, D. J. (2010). Gaussian09 Revision D.01, Gaussian Inc. Wallingford CT. In *Gaussian 09 Revision C.01*.

He, S., Song, J., Qu, J., & Cheng, Z. (2018). Crucial breakthrough of second near-infrared biological window fluorophores: design and synthesis toward multimodal imaging and theranostics. *Chemical Society Reviews*, *47*(12), 4258–4278. https://doi.org/10.1039/C8CS00234G

Hishikawa, H., Kaibori, M., Tsuda, T., Matsui, K., Okumura, T., Ozeki, E., & Yoshii, K. (2019). Near-infrared fluorescence imaging and photodynamic therapy with indocyanine green lactosomes has antineoplastic effects for gallbladder cancer. *Oncotarget*, *10*(54), 5622–5631. https://doi.org/10.18632/oncotarget.27193

Hong, G., Antaris, A. L., & Dai, H. (2017). Near-infrared fluorophores for biomedical imaging. *Nature Biomedical Engineering*, *1*(1), 0010. https://doi.org/10.1038/s41551-016-0010

Islam, R., Parves, M. R., Paul, A. S., Uddin, N., Rahman, M. S., Mamun, A. Al, Hossain, M. N., Ali, M. A., & Halim, M. A. (2020). A molecular modeling approach to identify effective antiviral phytochemicals against the main protease of SARS-CoV-2. *Journal of Biomolecular Structure and Dynamics*, 1–12. https://doi.org/10.1080/07391102.2020.1761883

Li, Y., Liu, S., Ni, H., Zhang, H., Zhang, H., Chuah, C., Ma, C., Wong, K. S., Lam, J. W. Y., Kwok, R. T. K., Qian, J., Lu, X., & Tang, B. Z. (2020). ACQ-to-AIE Transformation: Tuning Molecular Packing by Regioisomerization for Two-Photon NIR Bioimaging. *Angewandte Chemie International Edition*, *59*(31), 12822–12826. https://doi.org/10.1002/anie.202005785

Lin, H., Lin, Z., Zheng, K., Wang, C., Lin, L., Chen, J., & Song, J. (2021). Near-Infrared-II Nanomaterials for Fluorescence Imaging and Photodynamic Therapy. *Advanced Optical Materials*, *9*(9), 2002177. https://doi.org/10.1002/adom.202002177

Lokhande, K. B., Ballav, S., Yadav, R. S., Swamy, K. V., & Basu, S. (2022). Probing intermolecular interactions and binding stability of kaempferol, quercetin and resveratrol derivatives with PPAR-γ: docking, molecular dynamics and MM/GBSA approach to reveal potent PPAR- γ agonist against cancer. *Journal of Biomolecular Structure and Dynamics*, *40*(3), 971–981. https://doi.org/10.1080/07391102.2020.1820380

Mfouo-Tynga, I., & Abrahamse, H. (2015). Cell Death Pathways and Phthalocyanine as an Efficient Agent for Photodynamic Cancer Therapy. *International Journal of Molecular Sciences*, *16*(12), 10228–10241. https://doi.org/10.3390/ijms160510228

Miller, K. D., Nogueira, L., Mariotto, A. B., Rowland, J. H., Yabroff, K. R., Alfano, C. M., Jemal, A., Kramer, J. L., & Siegel, R. L. (2019). Cancer treatment and survivorship statistics, 2019. *CA: A Cancer Journal for Clinicians*, *69*(5), 363–385. https://doi.org/10.3322/caac.21565

Mishra, D., Maurya, R. R., Kumar, K., Munjal, N. S., Bahadur, V., Sharma, S., Singh, P., & Bahadur, I. (2021). Structurally modified compounds of hydroxychloroquine, remdesivir and tetrahydrocannabinol against main protease of SARS-CoV-2, a possible hope for COVID-19: Docking and molecular dynamics simulation studies. *Journal of Molecular Liquids*, *335*, 116185. https://doi.org/10.1016/j.molliq.2021.116185

Moriguchi, I., Hirono, S., Nakagome, I., & Hirano, H. (1994). Comparison of Reliability of log P Values for Drugs Calculated by Several Methods. *Chemical and Pharmaceutical Bulletin*, *42*(4), 976–978. https://doi.org/10.1248/cpb.42.976

Rubtsova, N. I., Hart, M. C., Arroyo, A. D., Osharovich, S. A., Liebov, B. K., Miller, J., Yuan, M., Cochran, J. M., Chong, S., Yodh, A. G., Busch, T. M., Delikatny, E. J., Anikeeva, N., & Popov, A. V. (2021). NIR Fluorescent Imaging and Photodynamic Therapy with a Novel Theranostic Phospholipid Probe for Triple-Negative Breast Cancer Cells. *Bioconjugate Chemistry*, *32*(8), 1852–1863. https://doi.org/10.1021/acs.bioconjchem.1c00295

Sun, Y., Lei, Z., & Ma, H. (2022). Twisted aggregation-induced emission luminogens (AIEgens) contribute to mechanochromism materials: a review. *Journal of Materials Chemistry C*. https://doi.org/10.1039/D2TC02512D

Surti, M., Patel, M., Adnan, M., Moin, A., Ashraf, S. A., Siddiqui, A. J., Snoussi, M., Deshpande, S., & Reddy, M. N. (2020). Ilimaquinone (marine sponge metabolite) as a novel inhibitor of SARS-CoV-2 key target proteins in comparison with suggested COVID-19 drugs: designing, docking and molecular dynamics simulation study. *RSC Advances*, *10*(62), 37707–37720. https://doi.org/10.1039/D0RA06379G

Trott, O., & Olson, A. J. (2009). AutoDock Vina: Improving the speed and accuracy of docking with a new scoring function, efficient optimization, and multithreading. *Journal of Computational Chemistry*, NA-NA. https://doi.org/10.1002/jcc.21334

Wang, D., Lee, M. M. S., Xu, W., Shan, G., Zheng, X., Kwok, R. T. K., Lam, J. W. Y., Hu, X., & Tang, B. Z. (2019). Boosting Non-Radiative Decay to Do Useful Work: Development of a Multi-Modality Theranostic System from an AIEgen. *Angewandte Chemie International Edition*, *58*(17), 5628–5632. https://doi.org/10.1002/anie.201900366

Wang, J., Zhang, L., & Li, Z. (2021). Aggregation-Induced Emission Luminogens with Photoresponsive Behaviors for Biomedical Applications. *Advanced Healthcare Materials*, *10*(24), 2101169. https://doi.org/10.1002/adhm.202101169

Xu, P., Kang, F., Yang, W., Zhang, M., Dang, R., Jiang, P., & Wang, J. (2020). Molecular engineering of a high quantum yield NIR-II molecular fluorophore with aggregation-induced emission (AIE) characteristics for in vivo imaging. *Nanoscale*, *12*(8), 5084–5090. https://doi.org/10.1039/C9NR09999A

Xu, S., Duan, Y., & Liu, B. (2020). Precise Molecular Design for High-Performance Luminogens with Aggregation-Induced Emission. *Advanced Materials*, *32*(1), 1903530. https://doi.org/10.1002/adma.201903530

Xu, W., Wang, D., & Tang, B. Z. (2021). NIR-II AIEgens: A Win–Win Integration towards Bioapplications. *Angewandte Chemie*, *133*(14), 7476-7487. https://doi.org/10.1002/ange.202005899

SUPPORTING INFORMATION

Bridging Molecular Docking to Molecular Dynamics to Enlighten Recognition Processes of Tailored D-A/D-A-D Types' AIEgens with HSA/BSA

Harun Nalçakan[1,*], Gülbin Kurtay[2,*]

[1]Department of Chemistry, Faculty of Science, Ankara University, 06100, Ankara, Turkey
[2]Department of Chemistry, Faculty of Science, Hacettepe University, 06800, Ankara, Turkey

Content

Table S1. Molecular structures and IUPAC names of the studied photosensitizers

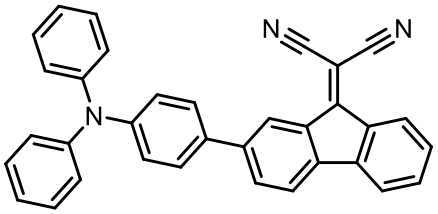
D_1A_1
2-(2-(4-(diphenylamino)phenyl)-9H-fluoren-9-ylidene)malononitrile
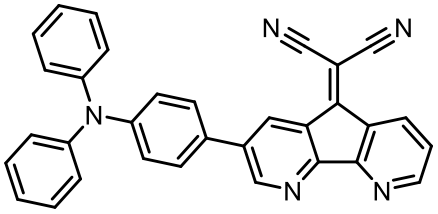
D_1A_2
2-(3-(4-(diphenylamino)phenyl)-5H-cyclopenta[2,1-b:3,4-b']dipyridin-5-ylidene)malononitrile
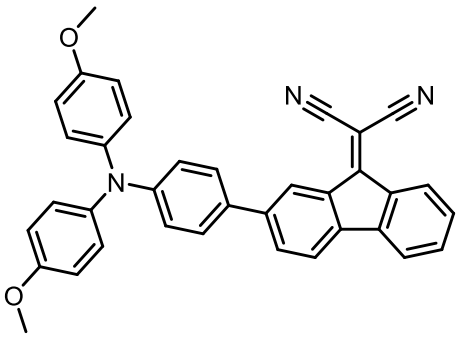
D_2A_1
2-(2-(4-(bis(4-methoxyphenyl)amino)phenyl)-9H-fluoren-9-ylidene)malononitrile
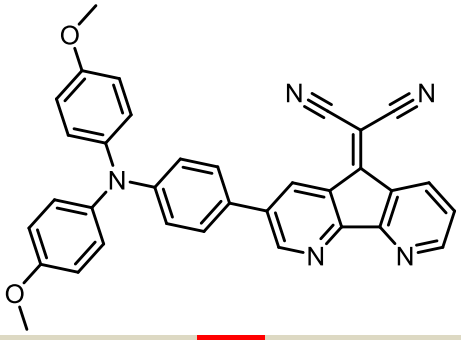
D_2A_2
2-(3-(4-(bis(4-methoxyphenyl)amino)phenyl)-5H-cyclopenta[2,1-b:3,4-b']dipyridin-5-ylidene)malononitrile

Table S1 *(cont.)*. Molecular structures and IUPAC names of the studied photosensitizers

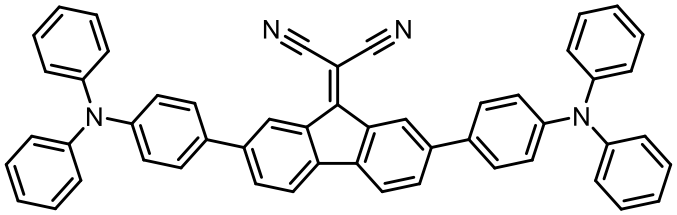
$D_1A_1D_1$
2-(2,7-bis(4-(diphenylamino)phenyl)-9H-fluoren-9-ylidene)malononitrile
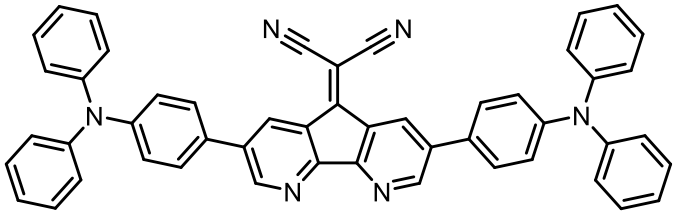
$D_1A_2D_1$
2-(3,7-bis(4-(diphenylamino)phenyl)-5H-cyclopenta[2,1-b:3,4-b']dipyridin-5-ylidene)malononitrile
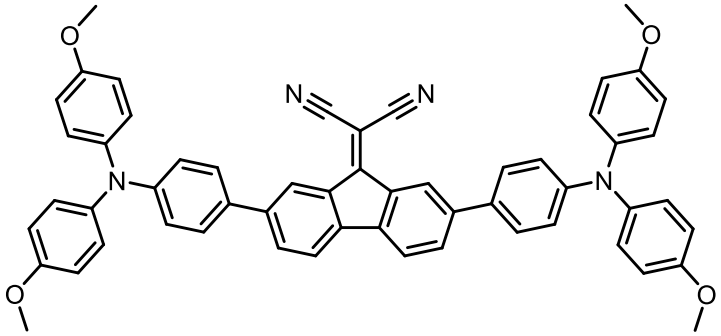
$D_2A_1D_2$
2-(2,7-bis(4-(bis(4-methoxyphenyl)amino)phenyl)-9H-fluoren-9-ylidene)malononitrile
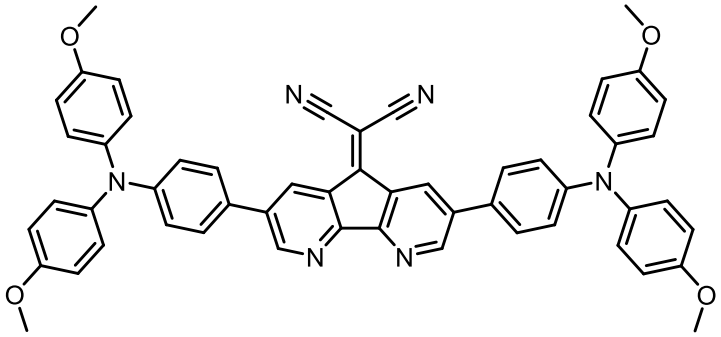
$D_2A_2D_2$
2-(3,7-bis(4-(bis(4-methoxyphenyl)amino)phenyl)-5H-cyclopenta[2,1-b:3,4-b']dipyridin-5-ylidene)malononitrile

Table S2. Interaction data of the studied ligands with BSA (PDB ID: 4F5S)

Ligands	Distance	Category	Type of Interactions	Residue Information
D_1-A_1	2.69	HB	C-HB	LYS136
	4.50	E	Pi-Ca	LYS136
	4.15	E	Pi-Ca	ARG185
	3.41	E	Pi-An	GLU125
	3.13	E	Pi-An	GLU125
	4.87	Other	Pi-S	MET184
	5.13	Hyd	Pi-Pi-T-Sh	TYR137
	4.99	Hyd	Am-Pi-St	MET184, ARG185
	3.72	Hyd	Pi-Al	LYS136
	5.31	Hyd	Pi-Al	LEU122
	4.62	Hyd	Pi-Al	LYS136
	3.72	Hyd	Pi-Al	LYS136
	4.76	Hyd	Pi-Al	LEU115
	5.29	Hyd	Pi-Al	PRO117
	5.24	Hyd	Pi-Al	LEU115
	4.24	Hyd	Pi-Al	PRO117
	5.38	Hyd	Pi-Al	ILE181
	4.04	Hyd	Pi-Al	ARG185
	5.48	Hyd	Pi-Al	VAL188
D_1-A_2	2.92	HB	CON-HB	LYS116
	2.40	HB	CON-HB	ASP118
	2.78	HB	C-HB	LEU115
	3.78	E	Pi-Ca	LYS132
	3.49	E	Pi-Ca	LYS136
	3.30	HB; E	Pi-Ca; Pi-Do HB	LYS136
	3.16	E	Pi-An	GLU125
	5.81	Hyd	Pi-Pi-St	TYR160
	4.45	Hyd	Pi-Al	LEU115
	4.84	Hyd	Pi-Al	LEU122
	5.42	Hyd	Pi-Al	LEU122
	4.60	Hyd	Pi-Al	LYS136
	4.13	Hyd	Pi-Al	LEU115
	4.88	Hyd	Pi-Al	PRO117
	4.19	Hyd	Pi-Al	LYS136
D_2-A_1	4.89	E	Pi-An	GLU424
	3.91	E	Pi-An	GLU424
	3.96	E	Pi-An	GLU424
	3.86	Hyd	Al	ALA193
	5.12	Hyd	Pi-Al	PRO420
	5.23	Hyd	Pi-Al	ILE522
	5.21	Hyd	Pi-Al	VAL423
	4.46	Hyd	Pi-Al	ILE522
	4.14	Hyd	Pi-Al	PRO420
	4.69	Hyd	Pi-Al	LEU189
	4.83	Hyd	Pi-Al	LEU189
D_2-A_2	2.73	HB; E	Pi-Ca; Pi-Do HB	LYS116
	3.07	E	Pi-An	GLU125
	4.60	Hyd	Al	LYS132
	5.09	Hyd	Al	LEU115
	4.91	Hyd	Pi-Al	TYR137
	5.38	Hyd	Pi-Al	LEU115
	5.46	Hyd	Pi-Al	LEU122
	3.65	Hyd	Pi-Al	LYS136
	4.43	Hyd	Pi-Al	LEU115

Abbreviations: Hydrophobic: Hyd, Electrostatic: E, Hydrogen Bond: HB, Conventional Hydrogen Bond: CON-HB, Carbon Hydrogen Bond: C-HB, Pi-Cation: Pi-Ca, Pi-Anion: Pi-An, Pi-Donor: Pi-Do, Alkyl: Al, Pi-Alkyl: Pi-Al, Pi-Pi T-Shaped: Pi-Pi T, Pi-Pi Stacked: Pi-Pi-St, Pi-Sulfur: Pi-S, Pi-Sigma: Pi-Sg, Amide-Pi Stacked: Am-Pi-St

Table S2. *(cont.)*. Interaction data of the studied ligands with BSA (PDB ID: 4F5S)

Ligands	Distance	Category	Type of Interactions	Residue Information
D_1-A_2-D_1	2.93	HB	CON-HB	LYS294
	3.43	E	Pi-Ca	ARG217
	4.00	E	Pi-Ca	LYS294
	3.65	E	Pi-Ca	LYS294
	4.16	Hyd	Pi-Al	ALA290
	5.30	Hyd	Pi-Al	LYS187
D_2-A_1-D_2	3.63	HB	C-HB	GLU182
	4.86	E	Pi-Ca	LYS114
	4.90	E	Pi-An	GLU424
	4.24	E	Pi-An	GLU424
	4.48	E	Pi-An	GLU424
	2.65	Hyd	Pi-Sg	LEU189
	2.84	Hyd	Pi-Sg	ILE522
	4.03	Hyd	Al	ARG185
	4.08	Hyd	Al	LYS504
	4.77	Hyd	Pi-Al	HIS145
	5.13	Hyd	Pi-Al	VAL423
	5.10	Hyd	Pi-Al	PRO420
	5.28	Hyd	Pi-Al	VAL423
	4.88	Hyd	Pi-Al	ILE522
	4.08	Hyd	Pi-Al	PRO420
	4.92	Hyd	Pi-Al	VAL423
	4.69	Hyd	Pi-Al	LEU189
	5.03	Hyd	Pi-Al	PRO420

Abbreviations: Hydrophobic: Hyd, Electrostatic: E, Hydrogen Bond: HB, Conventional Hydrogen Bond: CON-HB, Carbon Hydrogen Bond: C-HB, Pi-Cation: Pi-Ca, Pi-Anion: Pi-An, Pi-Donor: Pi-Do, Alkyl: Al, Pi-Alkyl: Pi-Al, Pi-Pi T-Shaped: Pi-Pi T, Pi-Pi Stacked: Pi-Pi-St, Pi-Sulfur: Pi-S, Pi-Sigma: Pi-Sg, Amide-Pi Stacked: Am-Pi-St

Table S2. *(cont.)*. Interaction data of the studied ligands with BSA (PDB ID: 4F5S)

Ligands	Distance	Category	Type of Interactions	Residue Information
D_2-A_2-D_2	2.91	HB	C-HB	THR526
	3.58	HB	C-HB	LEU189
	3.54	HB	C-HB	GLU182
	4.54	E	Pi-Ca	LYS114
	5.00	E	Pi-An	GLU424
	4.80	E	Pi-An	GLU424
	2.65	Hyd	Pi-Sg	LEU189
	2.72	Hyd	Pi-Sg	ILE522
	3.91	Hyd	Al	ALA193
	4.87	Hyd	Al	LEU189
	4.46	Hyd	Al	ARG185
	5.09	Hyd	Pi-Al	VAL423
	5.22	Hyd	Pi-Al	PRO420
	5.31	Hyd	Pi-Al	VAL423
	4.80	Hyd	Pi-Al	ILE522
	4.15	Hyd	Pi-Al	PRO420
	4.94	Hyd	Pi-Al	VAL423
	4.87	Hyd	Pi-Al	LEU189
	4.92	Hyd	Pi-Al	PRO420

Abbreviations: Hydrophobic: Hyd, Electrostatic: E, Hydrogen Bond: HB, Conventional Hydrogen Bond: CON-HB, Carbon Hydrogen Bond: C-HB, Pi-Cation: Pi-Ca, Pi-Anion: Pi-An, Pi-Donor: Pi-Do, Alkyl: Al, Pi-Alkyl: Pi-Al, Pi-Pi T-Shaped: Pi-Pi T, Pi-Pi Stacked: Pi-Pi-St, Pi-Sulfur: Pi-S, Pi-Sigma: Pi-Sg, Amide-Pi Stacked: Am-Pi-St

Table S3. Interaction data of the studied ligands with HSA (PDB ID: 4L9Q)

Ligands	Distance	Category	Type of Interactions	Residue Information
D_1-A_2	2.20	HB	CON-HB	TYR160
	2.61	HB	C-HB	PHE133
	4.65	E	Pi-Ca	LYS136
	5.84	Other	Pi-S	MET122
	5.27	Hyd	Pi-Al	LEU114
	5.13	Hyd	Pi-Al	PRO117
	4.99	Hyd	Pi-Al	LYS136
	5.24	Hyd	Pi-Al	LYS136
	4.92	Hyd	Pi-Al	LEU114
	5.46	Hyd	Pi-Al	LEU181
	4.47	Hyd	Pi-Al	ARG185
	4.34	Hyd	Pi-Al	ARG185
D_2-A_1	2.56	HB	CON-HB	ARG116
	2.55	HB	C-HB	PRO117
	2.44	HB	C-HB	GLY188
	4.15	HB; E	Pi-Ca; Pi-Do, HB	ARG185
	5.23	Hyd	Pi-Pi-St	PHE133
	5.28	Hyd	Pi-Pi-St	PHE133
	5.32	Hyd	Pi-Pi-St	PHE133
	5.65	Hyd	Pi-Pi-T-Sh	TYR137
	3.89	Hyd	Al	ILE141
	4.06	Hyd	Pi-Al	HIS145
	5.08	Hyd	Pi-Al	PHE148
	5.13	Hyd	Pi-Al	LYS136
	4.43	Hyd	Pi-Al	LYS136
	4.03	Hyd	Pi-Al	LYS136
	4.86	Hyd	Pi-Al	ILE141
	4.00	Hyd	Pi-Al	ARG185
	4.04	Hyd	Pi-Al	ARG185

Abbreviations: Hydrophobic: Hyd, Electrostatic: E, Hydrogen Bond: HB, Conventional Hydrogen Bond: CON-HB, Carbon Hydrogen Bond: C-HB, Pi-Cation: Pi-Ca, Pi-Anion: Pi-An, Pi-Donor: Pi-Do, Alkyl: Al, Pi-Alkyl: Pi-Al, Pi-Pi T-Shaped: Pi-Pi T, Pi-Pi Stacked: Pi-Pi-St, Pi-Sulfur: Pi-S, Pi-Sigma: Pi-Sg, Amide-Pi Stacked: Am-Pi-St

Table S3. ***(cont.)***. Interaction data of the studied ligands with HSA (PDB ID: 4L9Q)

Ligands	Distance	Category	Type of Interactions	Residue Information
D_2-A_2	2.77	HB	CON-HB	ARG221
	2.25	HB	CON-HB	ARG221
	4.17	E	Pi-Ca	LYS194
	4.19	E	Pi-Ca	LYS194
	4.21	E	Pi-An	ASP450
	4.66	Hyd	Pi-Pi-St	TYR451
	4.57	Hyd	Al	LYS189
	5.37	Hyd	Al	LYS431
	5.39	Hyd	Pi-Al	LYS194
	4.52	Hyd	Pi-Al	LYS194
	5.29	Hyd	Pi-Al	VAL342
	5.10	Hyd	Pi-Al	ALA190
	3.87	Hyd	Pi-Al	LYS435
	4.55	Hyd	Pi-Al	ALA190
	5.42	Hyd	Pi-Al	LYS431
	5.18	Hyd	Pi-Al	LYS435
D_1-A_1-D_1	2.52	HB	C-HB	MET122
	4.24	E	Pi-Ca	ARG185
	3.55	E	Pi-An	ASP128
	4.32	Hyd	Pi-Pi-St	PHE133
	5.29	Hyd	Pi-Pi-St	PHE133
	4.58	Hyd	Pi-Pi-St	PHE133
	5.30	Hyd	Pi-Pi-T-Sh	TYR137
	4.88	Hyd	Pi-Al	ALA125
	4.62	Hyd	Pi-Al	LYS136
	4.48	Hyd	Pi-Al	LYS136
	4.24	Hyd	Pi-Al	ALA125
	4.82	Hyd	Pi-Al	LYS136
	5.26	Hyd	Pi-Al	LEU181
	4.85	Hyd	Pi-Al	ARG185
	5.19	Hyd	Pi-Al	LEU114
	4.65	Hyd	Pi-Al	ARG116
	5.13	Hyd	Pi-Al	ALA125

Abbreviations: Hydrophobic: Hyd, Electrostatic: E, Hydrogen Bond: HB, Conventional Hydrogen Bond: CON-HB, Carbon Hydrogen Bond: C-HB, Pi-Cation: Pi-Ca, Pi-Anion: Pi-An, Pi-Donor: Pi-Do, Alkyl: Al, Pi-Alkyl: Pi-Al, Pi-Pi T-Shaped: Pi-Pi T, Pi-Pi Stacked: Pi-Pi-St, Pi-Sulfur: Pi-S, Pi-Sigma: Pi-Sg, Amide-Pi Stacked: Am-Pi-St

Table S3. ***(cont.)***. Interaction data of the studied ligands with HSA (PDB ID: 4L9Q)

Ligands	Distance	Category	Type of Interactions	Residue Information
D_1-A_2-D_1	2.46	HB	C-HB	MET122
	1.86	HB	C-HB	PHE133
	4.18	E	Pi-Ca	ARG185
	5.73	Hyd	Pi-Pi-St	TYR160
	5.08	Hyd	Pi-Al	ALA125
	4.53	Hyd	Pi-Al	LYS136
	4.48	Hyd	Pi-Al	LYS136
	4.37	Hyd	Pi-Al	ALA125
	4.59	Hyd	Pi-Al	LYS136
	4.86	Hyd	Pi-Al	ARG116
	5.24	Hyd	Pi-Al	LEU181
	5.36	Hyd	Pi-Al	LEU114
	5.11	Hyd	Pi-Al	ILE141
	5.10	Hyd	Pi-Al	ARG185
	4.89	Hyd	Pi-Al	ALA125
D_2-A_1-D_2	2.33	HB	C-HB	ARG116
	2.68	HB	C-HB	PRO117
	3.40	E	Pi-Ca	ARG185
	4.55	E	Pi-An	ASP128
	5.04	Hyd	Pi-Pi-St	PHE133
	5.02	Hyd	Pi-Pi-St	PHE133
	5.03	Hyd	Pi-Pi-St	PHE133
	3.75	Hyd	Al	ILE141
	4.35	Hyd	Pi-Al	HIS145
	5.19	Hyd	Pi-Al	PHE148
	4.81	Hyd	Pi-Al	LYS136
	4.21	Hyd	Pi-Al	LYS136
	4.08	Hyd	Pi-Al	LYS136
	5.18	Hyd	Pi-Al	LEU114
	4.91	Hyd	Pi-Al	ILE141
	4.10	Hyd	Pi-Al	ARG185
	4.96	Hyd	Pi-Al	ARG185
	5.03	Hyd	Pi-Al	ALA125

Abbreviations: Hydrophobic: Hyd, Electrostatic: E, Hydrogen Bond: HB, Conventional Hydrogen Bond: CON-HB, Carbon Hydrogen Bond: C-HB, Pi-Cation: Pi-Ca, Pi-Anion: Pi-An, Pi-Donor: Pi-Do, Alkyl: Al, Pi-Alkyl: Pi-Al, Pi-Pi T-Shaped: Pi-Pi T, Pi-Pi Stacked: Pi-Pi-St, Pi-Sulfur: Pi-S, Pi-Sigma: Pi-Sg, Amide-Pi Stacked: Am-Pi-St

Table S3. ***(cont.)***. Interaction data of the studied ligands with HSA (PDB ID: 4L9Q)

Ligands	Distance	Category	Type of Interactions	Residue Information
D_2-A_2-D_2	2.25	HB	CON-HB	MET297
	2.69	HB	C-HB	GLU293
	2.81	HB	C-HB	CYS447
	3.54	HB	C-HB	GLU291
	4.35	E	Pi-An	GLU187
	3.34	HB	Pi-Do, HB	ASN294
	3.88	Hyd	Al	ALA442
	5.37	Hyd	Al	MET297
	4.83	Hyd	Pi-Al	ALA190
	4.90	Hyd	Pi-Al	PRO338
	4.95	Hyd	Pi-Al	LYS443
	5.39	Hyd	Pi-Al	PRO338
	5.43	Hyd	Pi-Al	ALA442
	5.48	Hyd	Pi-Al	MET297
	5.11	Hyd	Pi-Al	PRO338

Abbreviations: Hydrophobic: Hyd, Electrostatic: E, Hydrogen Bond: HB, Conventional Hydrogen Bond: CON-HB, Carbon Hydrogen Bond: C-HB, Pi-Cation: Pi-Ca, Pi-Anion: Pi-An, Pi-Donor: Pi-Do, Alkyl: Al, Pi-Alkyl: Pi-Al, Pi-Pi T-Shaped: Pi-Pi T, Pi-Pi Stacked: Pi-Pi-St, Pi-Sulfur: Pi-S, Pi-Sigma: Pi-Sg, Amide-Pi Stacked: Am-Pi-St

Figure S2. Bioavailability radar representations of the investigated

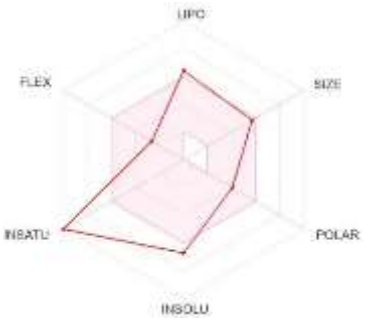

D_1A_2

D_2A_1

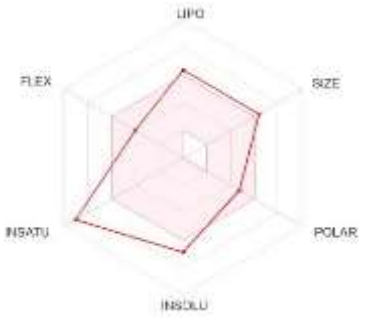

D_2A_2

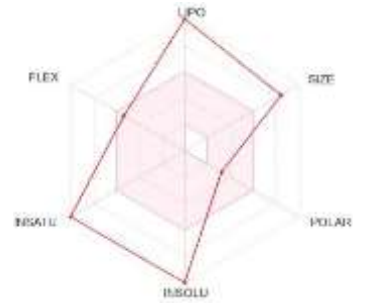

$D_1A_1D_1$

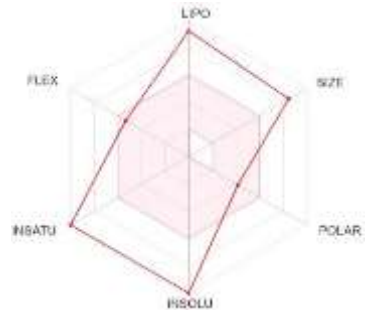

$D_1A_2D_1$

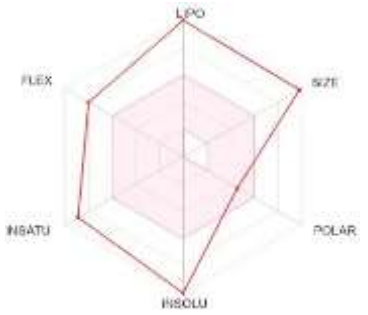

$D_2A_1D_2$

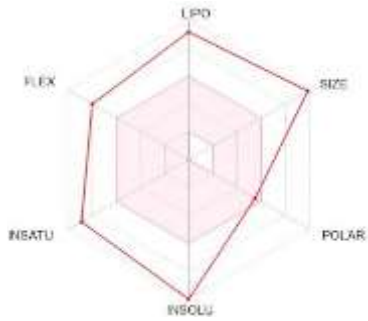

$D_2A_2D_2$

Figure S2. Binding poses and residue interactions of the investigated ligands with BSA (PDB ID: 4F5S)

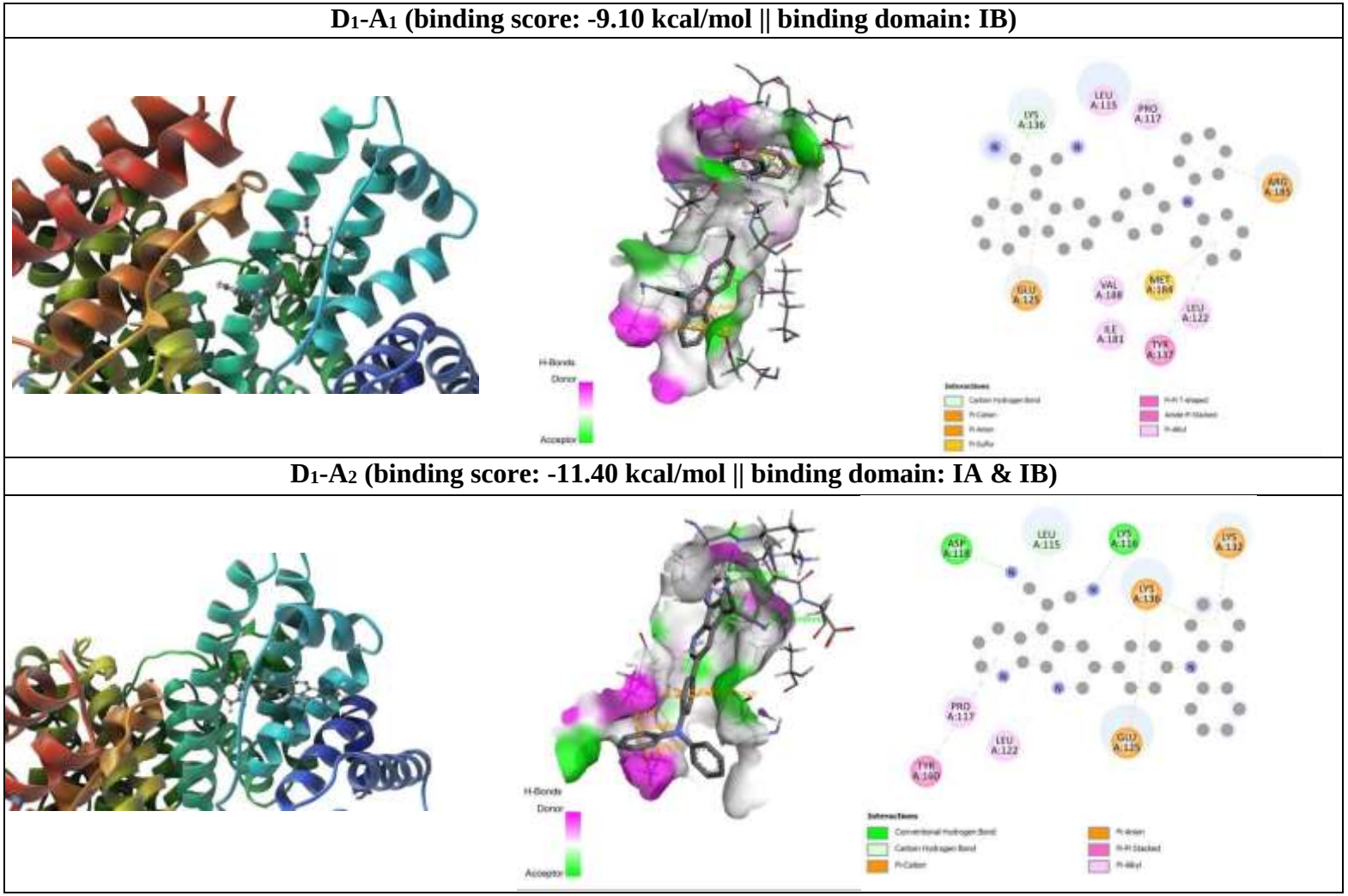

Figure S2. ***(cont.).*** Binding poses and residue interactions of the investigated ligands with BSA (PDB ID: 4F5S)

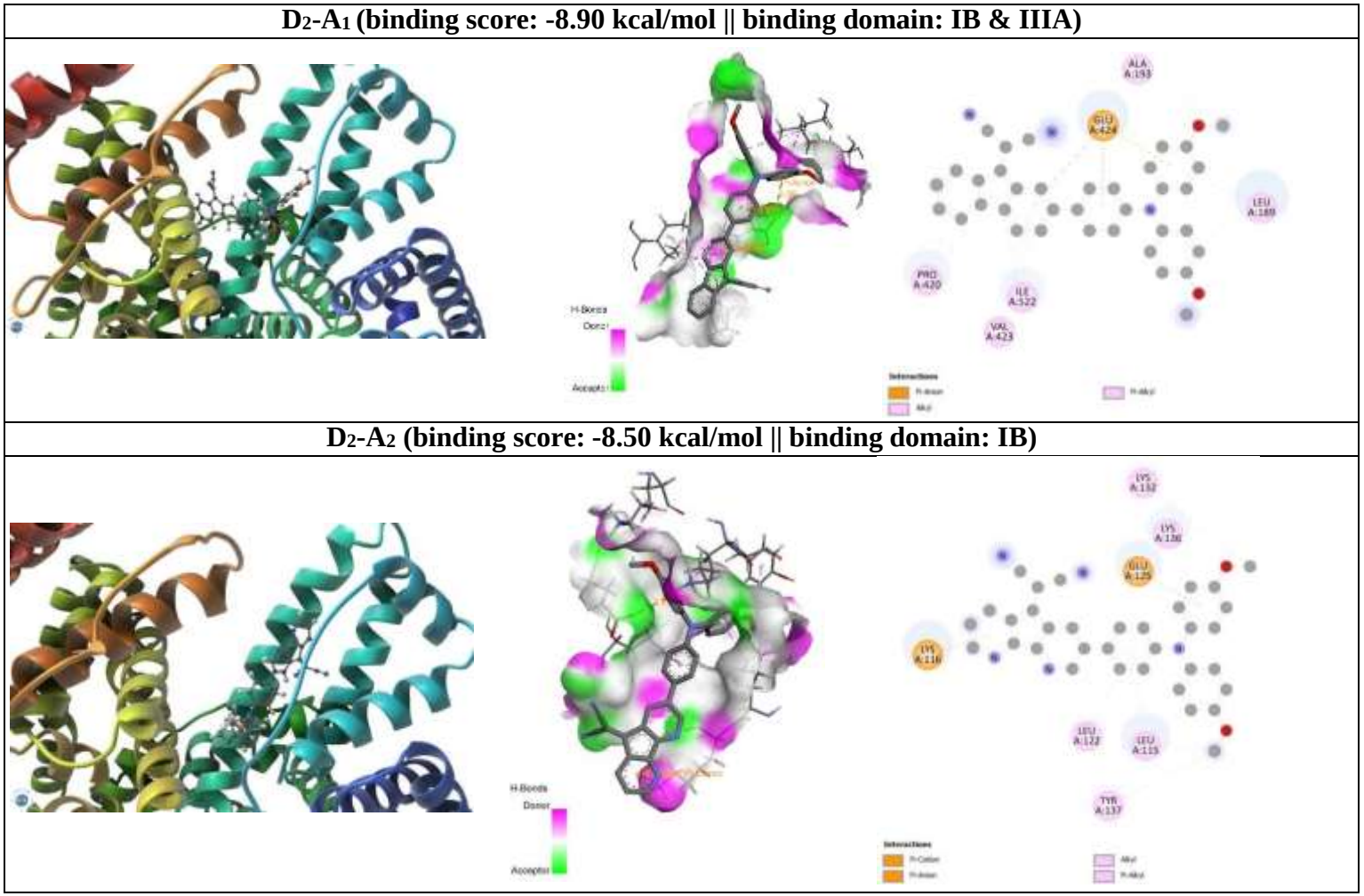

Figure S2. ***(cont.).*** Binding poses and residue interactions of the investigated ligands with BSA (PDB ID: 4F5S)

D_1-A_2-D_1 (binding score: -10.90 kcal/mol || binding domain: IB & IIIA)

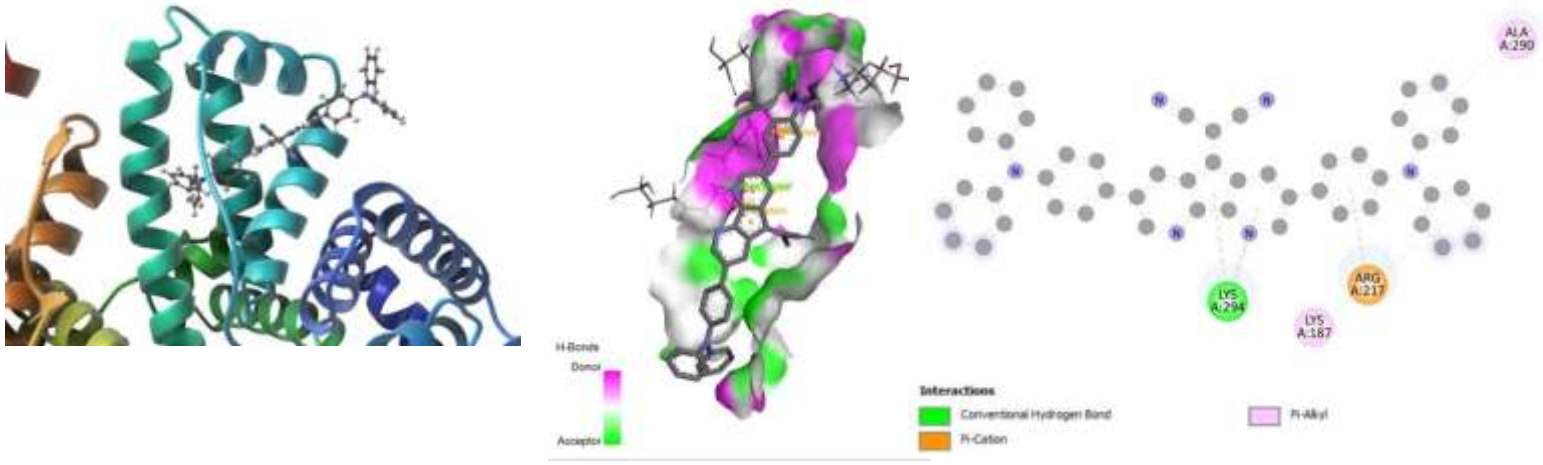

D_2-A_1-D_2 (binding score: -8.80 kcal/mol || binding domain: IB & IIIA & IIIB)

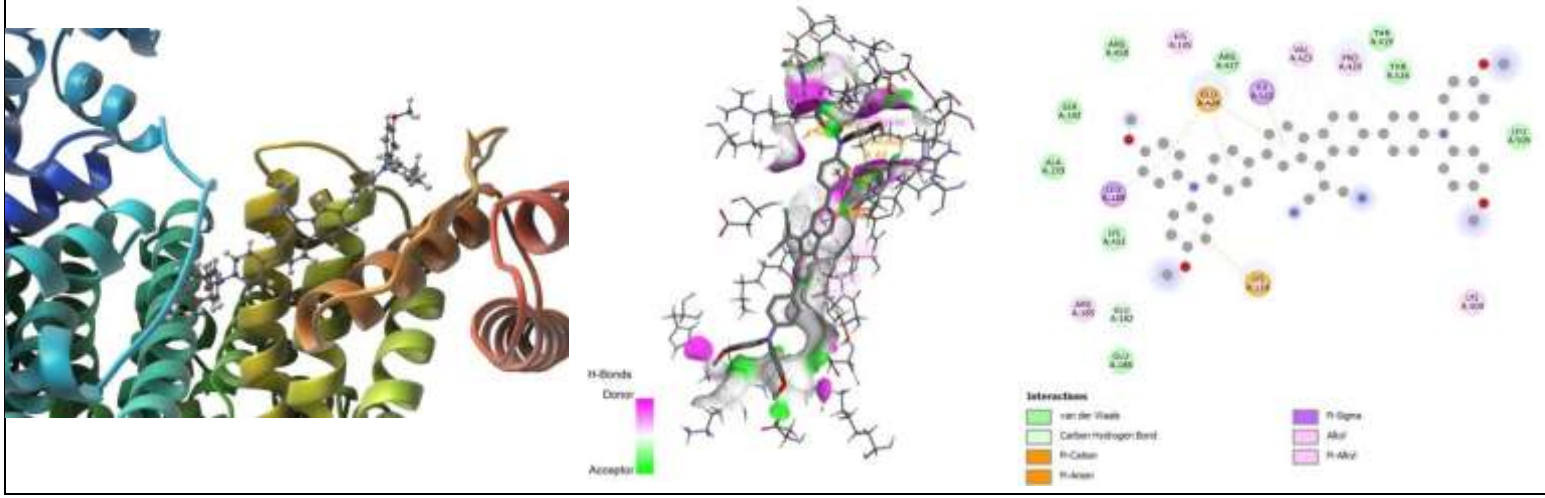

Figure S2. ***(cont.).*** Binding poses and residue interactions of the investigated ligands with BSA (PDB ID: 4F5S)

D_2-A_2-D_2 (binding score: -8.50 kcal/mol || binding domain: IB & IIIA & IIIB)

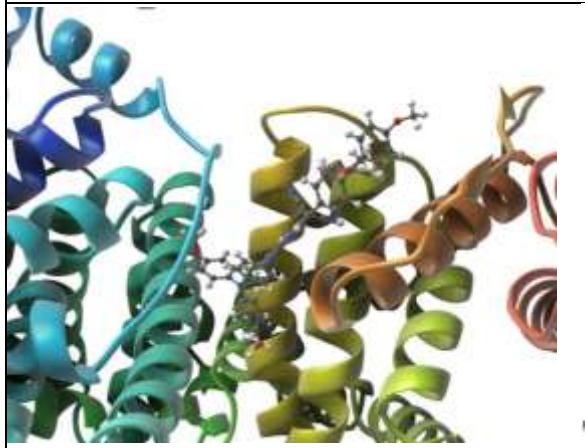

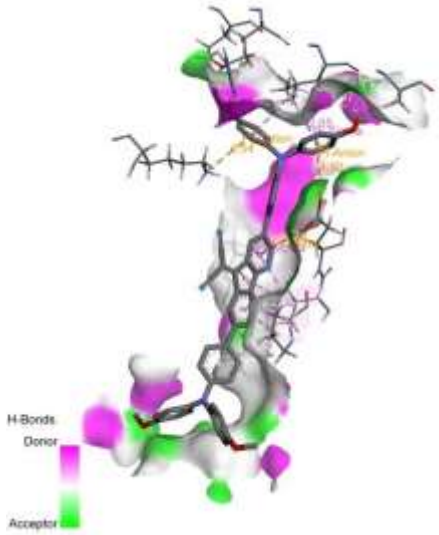

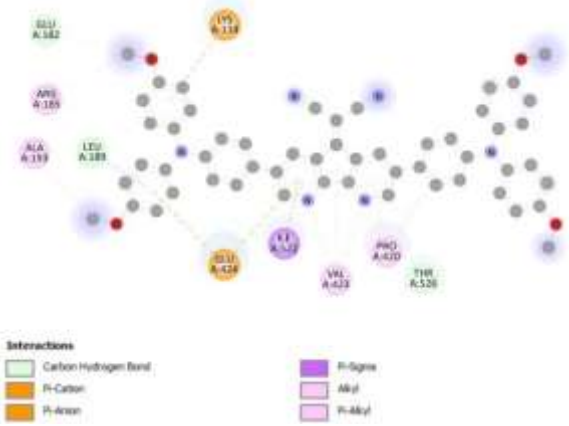

Figure S3. Binding poses and residue interactions of the investigated ligands with HSA (PDB ID: 4L9Q)

D_1-A_2 (binding score: -9.90 kcal/mol || binding domain: IB)

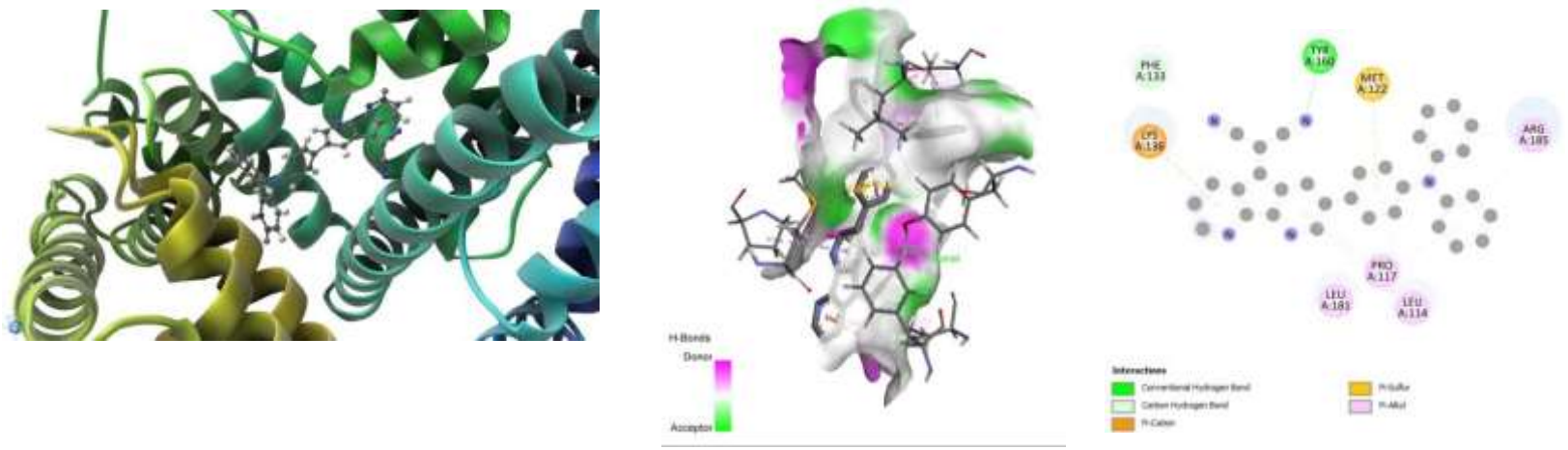

D_2-A_1 (binding score: -10.00 kcal/mol || binding domain: IB)

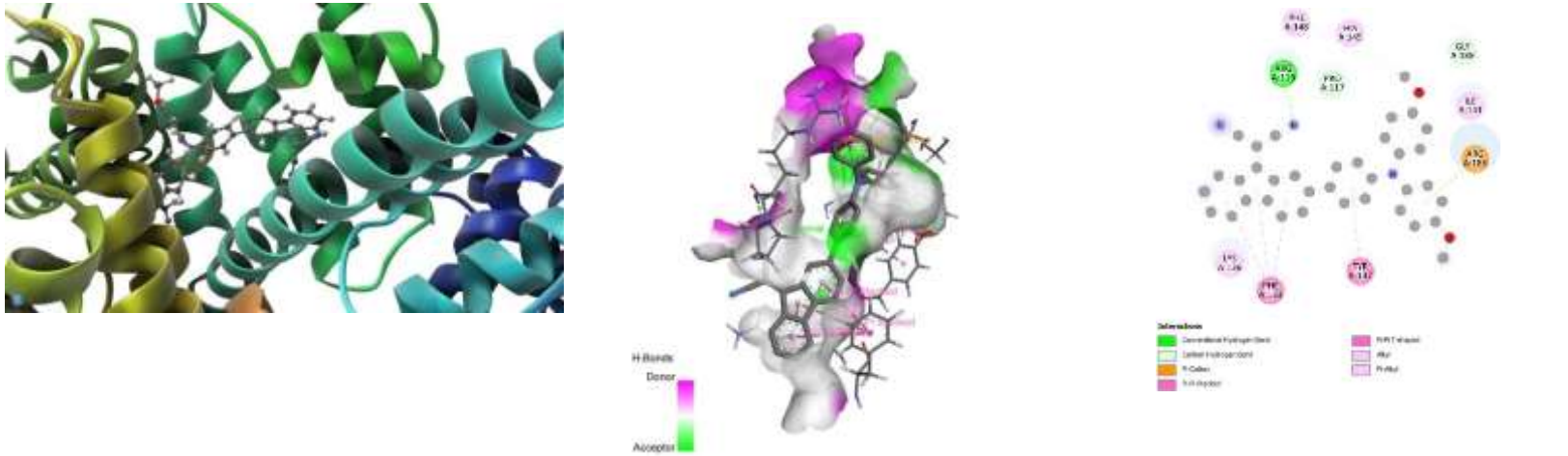

Figure S3. ***(cont.).*** Binding poses and residue interactions of the investigated ligands with HSA (PDB ID: 4L9Q)

D_2-A_2 (binding score: -9.40 kcal/mol || binding domain: IB & IIIA)

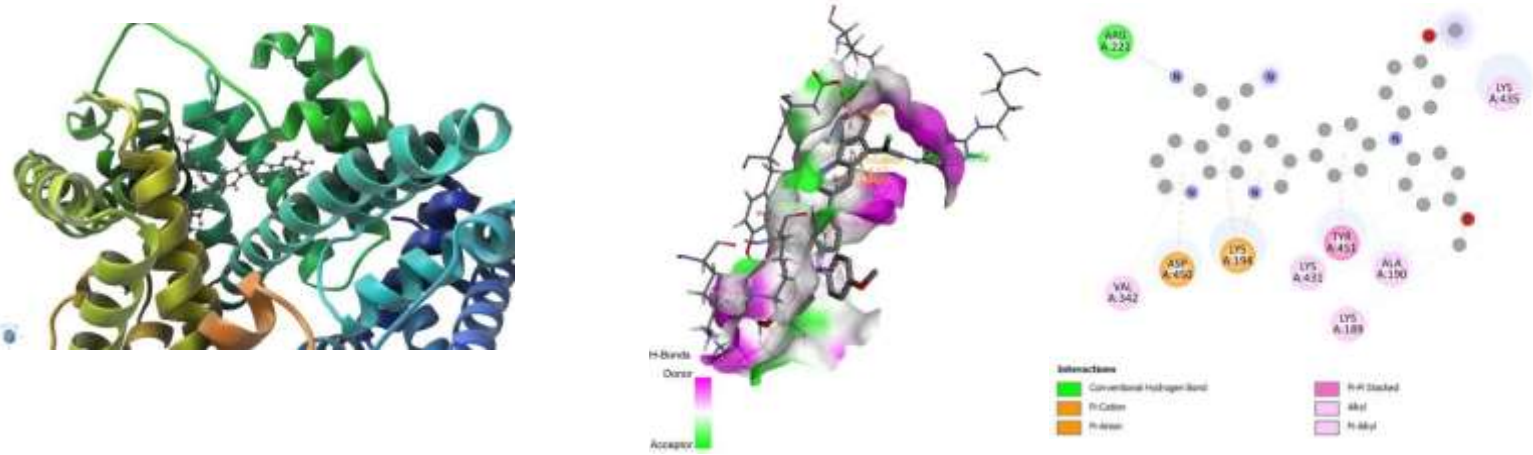

D_1-A_1-D_1 (binding score: -10.10 kcal/mol || binding domain: IB)

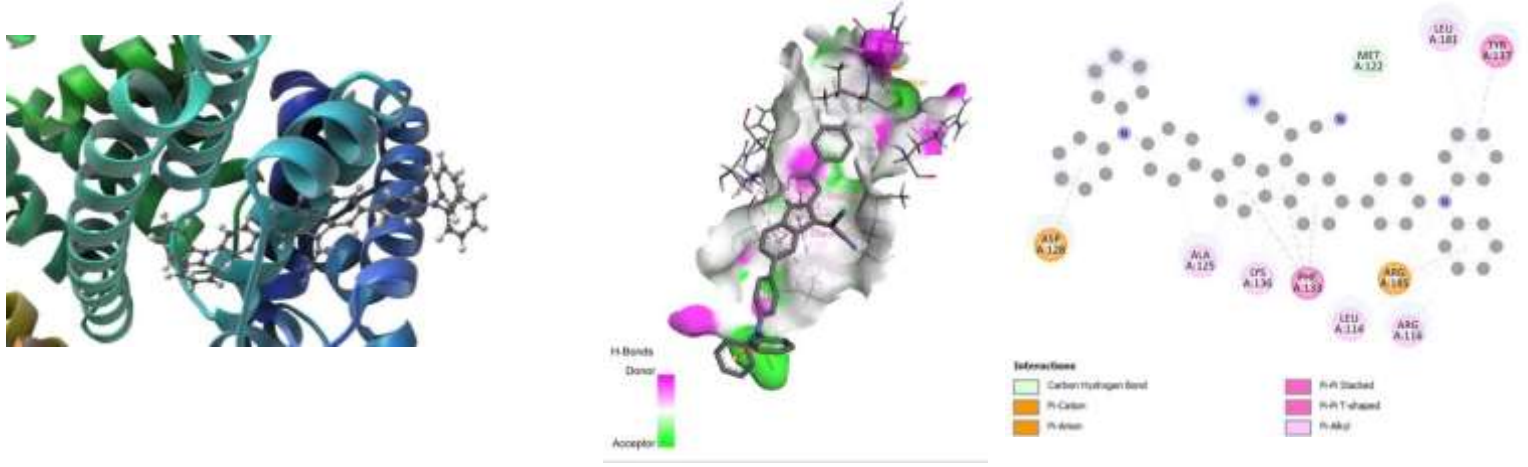

Figure S3. ***(cont.).*** Binding poses and residue interactions of the investigated ligands with HSA (PDB ID: 4L9Q)

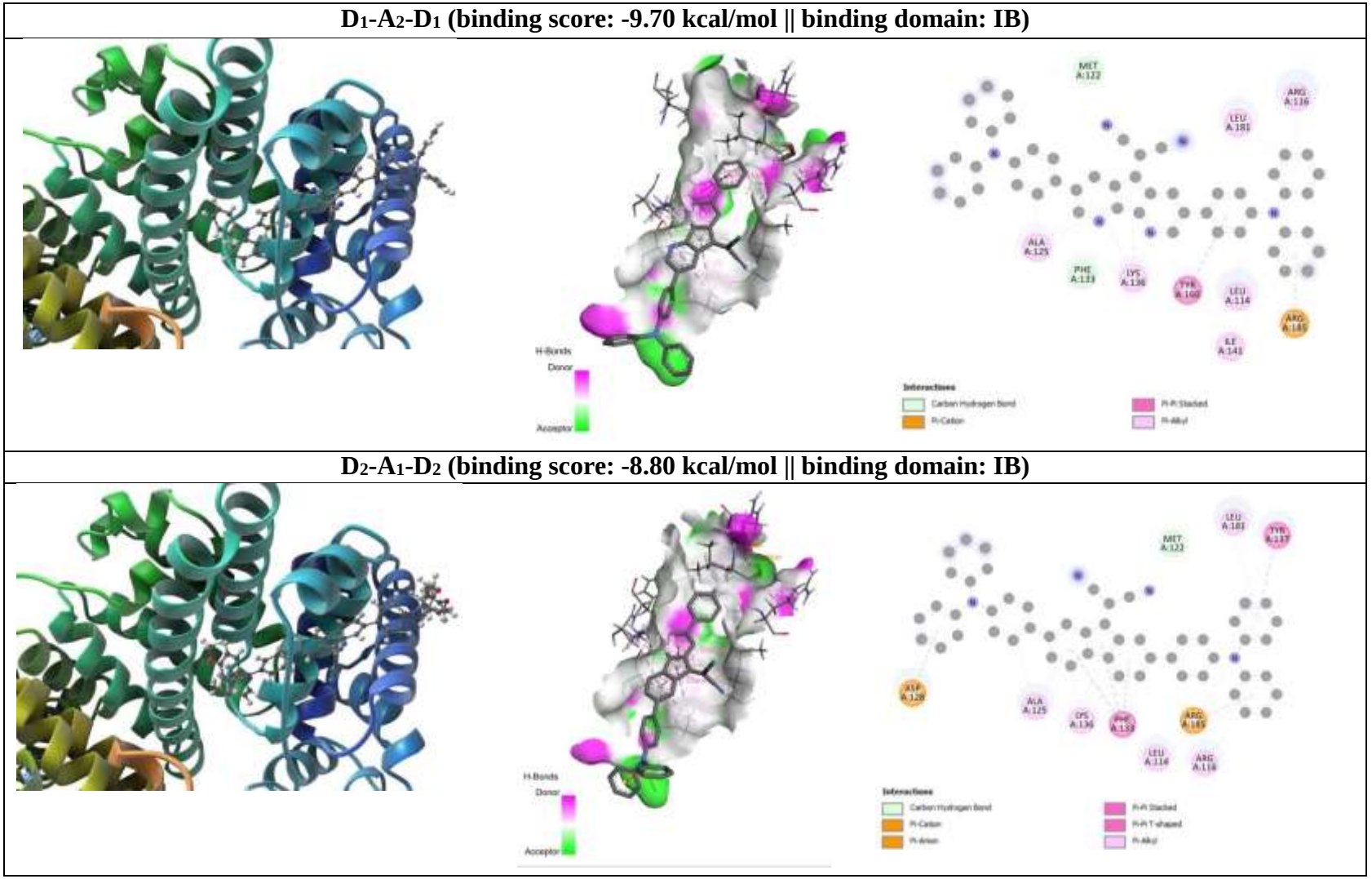

Figure S3. ***(cont.).*** Binding poses and residue interactions of the investigated ligands with HSA (PDB ID: 4L9Q)

D_2-A_2-D_2 (binding score: -8.40 kcal/mol || binding domain: IB & IIIA)